Corrosion inhibition of copper alloys by organic compounds

DELFT UNIVERSITY OF TECHNOLOGY

MASTER THESIS REPORT

(MS53100)

Author: Li Xiang (studentnumber: 4746821)

Supervisor: Dr. J.M.C. Mol

Co-Supervisor: Dr. P. Taheri

Faculty of Mechanical, Maritime and Materials Engineering

Materials Science and Engineering

September 30, 2019

Abstract

Copper and copper alloys have been used widely in different applications, such as electric power transmissions and heat exchanges. However, they are susceptible to corrosion in different environments leading to damages and catastrophic failures. Different corrosion-inhibition strategies are used to retard corrosion of copper and copper alloys. Among them, corrosion inhibitors are successfully used to inhibit their corrosion.

This thesis focuses on the corrosion inhibition of brasses (the copper- zinc binary alloys) using two kinds of organic inhibitors, namely 2-mercapto-1-methyl-benzimidazole (1H-HB-2T) and 2-mercapto-benzimidazole (MBI). Corrosion inhibition of the substrates using the inhibitors were screened using linear polarization resistance (LPR) measurements. Subsequently, electrochemical impedance spectroscopy (EIS) was used to study the detailed corrosion inhibition processes and mechanisms. Finally, two modes (RAS and ATR) of Fourier transform infrared spectroscopy (FTIR) were adopted for in-situ and ex-situ tests to study the adsorption mechanisms of inhibitor molecules on the surfaces.

The research results showed that: (1) the composition (phase type) of the brass controls the interaction of inhibitor on surfaces; (2) an increased Zn content of brass leads to a decreased corrosion resistance; (3) 2-mercapto-1-methyl-benzimidazole (1H-HB-2T) exhibits better corrosion efficiency than 2-mercapto-benzimidazole (MBI) indicating the importance of the methyl functional group to increase the inhibitor's efficiency; (4) 1H-HB-2T exhibits a spontaneous structure transformation from thiol to thione and (5) within a maximum 5-hour exposure, the adsorption of the inhibitors to the metal surface is complete.

Contents

1 Introduction **1**

1.1 Corrosion of copper and brasses 1

1.2 Corrosion mechanisms of copper and brasses 1

1.2.0.1 Corrosion mechanisms of Pure Copper 1

1.2.0.2 Corrosion mechanisms of brasses 3

1.3 Corrosion inhibitors 6

1.4 Aims of the thesis 10

2 Experiments **11**

2.1 Experiment materials 11

2.2 Electrochemical measurements 13

2.2.1 Linear Polarization Resistance (LPR) 13

2.2.2 Electrochemical Impedance Spectroscopy (EIS) 18

2.3 Fourier Transform Infrared Spectroscopy(FTIR) 23

2.3.1 Ex-situ FTIR 27

2.3.2 In-situ FTIR 27

3 Results and discussion **29**

3.1 Electrochemical measurements 29

3.1.1 Linear Polarization Resistance (LPR) 32

3.1.1.1 Specimens in 1 mmol/L MBI solution 32

3.1.1.2 Specimens in 1 mmol/L 1H-HB-2T solution 36

3.1.1.3 Preselection of specimens 40
3.1.2 Electrochemical Impedance Spectroscopy (EIS) 42
3.1.2.1 Pure Cu in 1 mmol/L MBI solution 43
3.1.2.2 50% Zn brass in 1 mmol/L MBI solution 45
3.1.2.3 Pure Zn in 1 mmol/L MBI solution 47
3.1.2.4 Pure Cu in 100ml 1 mM 1H-HB-2T solution 49
3.1.2.5 50% Zn brass in 100ml 1 mM 1H-HB-2T solution 51
3.1.2.6 Pure Zn in 100ml 1 mM 1H-HB-2T solution 53
3.1.3 Summary of electrochemical measurements 55
3.2 Fourier Transform Infrared Spectroscopy(FTIR) 55
3.2.1 Ex-situ Fourier Transform Infrared Spectroscopy(FTIR) 57
3.2.1.1 The ex-situ FTIR spectrum in 1 mM MBI THF solution 57
3.2.1.2 The ex-situ FTIR spectrum in 1 mM 1H-HB-2T THF solution 58
3.2.2 In-situ Fourier Transform Infrared Spectroscopy(FTIR) 59
3.2.2.1 The in-situ FTIR spectrum of Pure Cu in 1 mM MBI THF solution 59
3.2.2.2 The in-situ FTIR spectrum of Pure Cu in 1 mM 1H-HB-2T THF solution 61
3.2.2.3 The in-situ FTIR spectrum of Pure Zn in 1 mM MBI THF solution 63
3.2.2.4 The in-situ FTIR spectrum of Pure Zn in 1 mM 1H-HB-2T THF solution 65
3.2.3 Summary of FTIR measurements 66

4 Conclusion **67**

5 Future work **68**

6 Acknowledgement **69**

List of Figures

1 Pourbaix diagram for copper water system at 25 degrees Celsius. Domain for stability of water shown by dotted lines. 2

2 Cu-Zn equilibrium phase diagram 3

3 Typical pitting corrosion phenomenon on the admiralty brass condenser tube 4

4 Metallographic cross-section through the wall of a pipe after 12 months of service in seawater. Dezincification of M70 alloy (Cu 69–71 %, rest Zn) reaches half of the wall thickness. 5

5 Photomicrograph of cracks in annealed 70 Cu 30 Zn brass, in sulfate solution which contains ammonia ions. 5

6 Theoretical potentiostatic polarization diagram: electrochemical behavior a metal on a solution containing an anodic (top left) or cathodic (top left) or both side (bottom) inhibitor (a) compared to the same solution without the inhibitor (b). 7

7 Illustration of the mechanism of actuation of the organic inhibitor: acting through adsorption of the inhibitor on the metal surface. Where the Inh represents the inhibitor molecules. 8

8 2-Mercaptobenzimidazole (MBI) structure. 11

9 1-Methyl-1H-benzimidazole-2-thiol (1H-HB-2T) structure. 12

10 Examples of transformation from thiol to thione. 12

11 Possible transformation of 1H-HB-2T from thiol to thione. 13

12 Schematic of the LPR fitting. 15

13 Sample configurations used for LPR measurements. 16

14 The three-electrode cell system. 17

15 LPR software setup. 18

16 Sinusoidal current response in a Linear System. 19

17 The parallel RC circuit structure. 20

18 Nyquist plot for a parallel RC circuit with R = 100 Ω and C = 1 μF. 21

19 Bode plots for a parallel RC circuit with R = 100 Ω and C = 1 μF. 21

20 Sample configuration of EIS measurements 22

21 EIS software setup. 23

22 Schematic of a typical FTIR imaging spectrometer 24

23 A fringing example in FTIR. 25

24 Optical configurations of surface-sensitive infrared techniques. (top): RAS, (bottom): ATR 26

25 The NICOLET 6700 FTIR machine. 27

26 The configuration of in-situ FTIR accessory. 28

27 Two simple models of hydrated Cu^{2+} ion, i.e., $[Cu(H_2O)_4]^{2+}_{(aq)}$ and $[Cu(H_2O)_4 \cdot 2(H_2O)]^{2+}_{(aq)}$. 31

28 Models of MBI forming a complex with hydrated Cu^{2+} ion, i.e., $[MBI\text{-}Cu(H_2O)_3]^{2+}_{(aq)}$ and $[MBI\text{-}Cu(H_2O)_3 \cdot 2(H_2O)]^{2+}_{(aq)}$. 31

29 Surface appearance after corrosion in the 1H-HB-2T solution. 32

30 Polarization resistance values of specimens immersed in 100ml 1 mM MBI solution. 33

31 Inhibition efficiencies of group 1 specimens immersed in 100ml 1 mM MBI solution. 34

32 Inhibition efficiencies of group 2 specimens immersed in 100ml 1 mM MBI solution. 35

33 Average polarization resistances of specimens immersed in 100ml 1 mM MBI solution. 36

34 Polarization resistance values of specimens immersed in 100ml 1 mM 1H-HB-2T solution. 37

35 Inhibition efficiencies of group 1 specimens immersed in 100ml 1 mM 1H-HB-2T solution. 38

36 Inhibition efficiencies of group 2 specimens immersed in 100ml 1 mM 1H-HB-2T solution. 39

37 Average polarization resistances of specimens immersed in a 100ml 1 mM MBI solution. 40

38 Polarization resistances of Cu immersed in 100ml 1 mM MBI and 1H-HB-2T solutions. 41

39 Polarization resistances of 50% Zn brass immersed in 100ml 1 mM MBI and 1H-HB-2T solutions. 41

40 Polarization resistances of Zn immersed in 100ml 1 mM MBI and 1H-HB-2T solutions. 42

41 Nyquist plot of pure Cu in 100ml 1 mM MBI solution for 50 hours. 44

42 Bode plots of pure Cu in 100ml 1 mM MBI solution for 50 hours. 45

43 Nyquist plot of 50% Zn brass in 100ml 1 mM MBI solution for 50 hours. . . . 46

44 Bode plots of 50% Zn brass in 100ml 1 mM MBI solution for 50 hours. 47

45 Nyquist plot of pure Zn in 100ml 1 mM MBI solution for 50 hours. 48

46 Bode plots of pure Zn in 100ml 1 mM MBI solution for 50 hours. 49

47 Nyquist plot of pure Cu in 100ml 1 mM 1H-HB-2T solution for 50 hours. . . . 50

48 Bode plots of pure Cu in 100ml 1 mM 1H-HB-2T solution for 50 hours. 51

49 Nyquist plot of 50% Zn brass in 100ml 1 mM 1H-HB-2T solution for 50 hours. 52

50 Bode plots of 50% Zn brass in 100ml 1 mM 1H-HB-2T solution for 50 hours. . 53

51 Nyquist plot of pure Zn in 100ml 1 mM 1H-HB-2T solution for 50 hours. . . . 54

52 Bode plots of pure Zn in 100ml 1 mM 1H-HB-2T solution for 50 hours. 55

53 Optimized structures of MBI molecules adsorbed on Cu(1 1 1) (left panels) and the [MBI–Cu_{ad}] monomer complex (right panels). Color coding of atoms is also indicated: H is cyan, C is yellow, N is sky-blue, and Cu is colored copper-brown with color becoming darker as going from surface toward the bulk. Bond lengths are specified in Åunits. 56

54 Ex-situ FTIR spectra of 1 mmol/100ml MBI solution. 58

55 Ex-situ FTIR spectra of 1 mmol/100ml 1H-HB-2T THF solution. 59

56 In-situ FTIR spectra of Cu in 100ml 1 mM MBI solution. 60

57 Peak intensity values of Cu from MBI FTIR spectra. 61

58 In-situ FTIR spectra of Cu in 100ml 1 mM 1H-HB-2T solution. 62

59 Peak intensity values of Cu from 1H-HB-2T FTIR spectra. 63

60 In-situ FTIR spectra of Zn in 100ml 1 mM MBI solution. 64

61 Peak intensity values of Zn from MBI FTIR spectra. 64

62 In-situ FTIR spectra of copper in 100ml 1 mM 1H-HB-2T solution. 65

63 Peak intensity values of Zn from 1H-HB-2T FTIR spectra. 66

List of Tables

1 Brass types. 4

2 Copper, zinc and brass samples. 11

3 MBI physicochemical information. 12

4 1H-HB-2T physicochemical information. 12

5 Electrolyte constitutes for electrochemical measurements. 13

6 LPR measurement time after the start of each experiment. 18

7 EIS measurement time after the start of each experiment. 22

8 R_{ct} obtained from the Nyquist plot. 45

9 R_{ct} obtained from the Nyquist plot. 47

10 R_{ct} obtained from the Nyquist plot. 49

11 R_{ct} obtained from the Nyquist plot. 51

12 R_{ct} obtained from the Nyquist plot. 53

13 R_{ct} obtained from the Nyquist plot. 55

14 Infrared absorption frequencies of functional groups. 56

1 Introduction

1.1 Corrosion of copper and brasses

Copper is a soft, malleable and ductile metal with very high thermal and electrical conductivity. Owing to its ready availability in nature, it has a long usage history since the prehistoric age civilization. In moderate society, it still plays roles in both industrial application and daily life. One evidence is that copper wire is everywhere. Moreover, the alloying of copper provides it better physical and chemical properties and make it workable in wider fields. One of the most successful copper alloys is copper-zinc alloys, also called brasses. Brasses show enhanced properties such as better strength and machinability, higher thermal and electrical conduction, better corrosion and wear resistance. By varying Cu-Zn proportion, specific brasses can be designed to meet different working requirements.

As for Cu and brasses, one of the problems which could threaten their usage safety is corrosion. Normally, copper and copper alloys belong to the group of metal material which have sufficient corrosion-resistance. However, under specific conditions, for instance, brass valves in fast-flowing water or when exposed to some pollutants in water will corrode seriously. Such a corrosion phenomenon may cause catastrophic damage and therefore, cannot be ignored.

1.2 Corrosion mechanisms of copper and brasses

According to the American Society for Testing and Materials' corrosion glossary, the definition of corrosion could be referred to as "the chemical or electrochemical reaction between a material, usually a metal, and its environment that produces a deterioration of the material and its properties" [1] which includes, for example, the deliberate anodic dissolution of zinc in cathodic protection and electroplating as well as the spontaneous gradual wastage of zinc roofing sheet resulting from atmospheric exposure [2]. In this thesis, the term corrosion is restricted to chemical attack of metals and we only concentrate on the corrosion of copper and brasses.

1.2.0.1 Corrosion mechanisms of Pure Copper

The chemical performance of copper depends on its position as the penultimate element in the first transition series. Following the preceding sequence, the configuration of the outer

electrons in the free copper atom might be expected to be $(3d)_9(4s)_2$, but due to the stability of the completed d shell, the actual configuration is $(3d)_{10}(4s)_1$. Hence, copper commonly exists in two oxidation states Cu(I) and Cu(II). [3]

There is an equilibrium between oxidation states Cu(I) and Cu(II),

$$2\,Cu^{I} = Cu + Cu^{II}$$

In aqueous solution, Cu^{+}(aq) ion can exist only in a very low concentration. [3]

$$2\,Cu^{+}\,(aq) = Cu^{2+}\,(aq) + Cu\,(s)$$

The corresponding reaction for solid oxides is not spontaneous, Cu_2O(s) is stabilized by the environment of oxygen ions and the relative stability of the oxides is determined by prevailing temperatures and oxygen potential. [3]

$$Cu_2O(s) = CuO(s) + Cu\,(s)$$

In solution, since copper is a noble metal that cannot react with pure water directly, copper cannot corrode with the revolution of hydrogen in quiescent water. And it also is stable in dilute non-oxidizing and non-complexing acids in absence of oxygen. Only highly oxidizing solutions such as concentrated nitric acid could corrode copper. Detailed relationship between the potential, PH and corrosion products of copper in water solution is concluded in its Pourbaix diagram shown in Figure 1. [3]

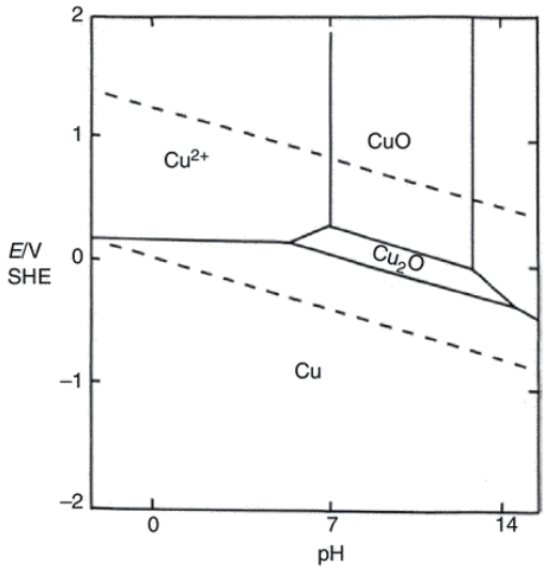

Figure 1: Pourbaix diagram for copper water system at 25 degrees Celsius. Domain for stability of water shown by dotted lines. [3]

As for atmospheric corrosion of copper, on exposure to clean dry air at ambient temperatures initially, copper could form a protective thin film according to the Cabrera–Mott theory. In the ordinary air condition and a room temperate, it tarnishes and the tarnish is thicker and more unsightly. If the air is polluted by sulfur dioxide, probably because sulfur ions incorporated in the film raise the concentration of cation vacancies, hence, the activation energy for the formation of the oxide is reduced and the critical thickness at which continuing oxidation is not detectable increases. [3, 4]

1.2.0.2 Corrosion mechanisms of brasses

Copper-zinc alloys, i.e. brasses, are known and utilized since early human society. They are mechanically stronger compared with pure copper, easier to be produced and machine. The copper-zinc binary phase diagram is shown below in Figure 2 [5]. A summary of the data extracted from Figure 3 is shown in Table.1 [6].

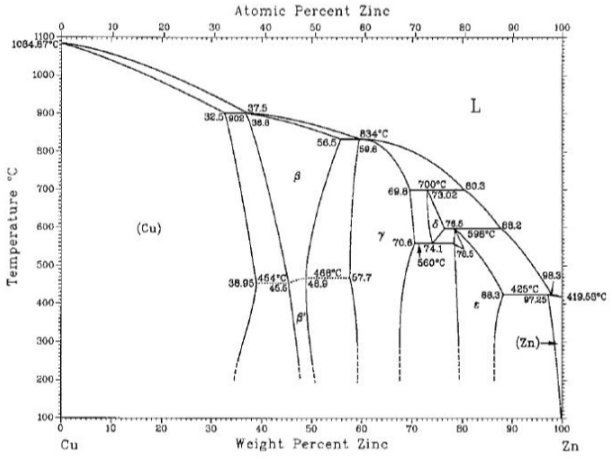

Figure 2: Cu-Zn equilibrium phase diagram. [5]

The alloying of the zinc element essentially changes copper's corrosion-resistant ability. In general, the increase of zinc content reduces alloys' corrosion resistance. As for different corrosion types, brasses are especially susceptible to pitting, dealloying, and Stress Corrosion Cracking which are introduced below.

Pitting corrosion can be also initiated by the same mechanisms as for pure copper. And susceptibility of brass to pitting corrosion is insensitive for its zinc content and microstructure. An pitting corrosion morphology is shown below.

Table 1: Brass types. [6]

Class	Proportion by weight(%)		Note
	Copper	Zinc	
Alpha brasses	>65	<35	Alpha brasses are malleable, can be worked cold, and are used in pressing, forging, or similar applications. They contain only one phase, with face-centered cubic crystal structure. With their high proportion of copper, these brasses have a more golden hue than others.
Alpha-beta brasses	55–65	35–45	Also called duplex brasses, these are suited for hot working. They contain both α and β' phases; the β'-phase is body-centered cubic and is harder and stronger than α. Alpha-beta brasses are usually worked hot. The higher proportion of zinc means these brasses are brighter than alpha brasses.
Beta brasses	50–55	45–50	Beta brasses can only be worked hot, and are harder, stronger, and suitable for casting. The high zinc-low copper content means these are some of the brightest and least-golden of the common brasses.
Gamma brasses	33–39	61–67	There are also Ag-Zn and Au-Zn gamma brasses, Ag 30–50%, Au 41%.
White brasses	<50	>50	These are too brittle for general use. The term may also refer to certain types of nickel silver alloys as well as Cu-Zn-Sn alloys with high proportions (typically 40%+) of tin and/or zinc, as well as predominantly zinc casting alloys with copper additives. These have virtually no yellow coloring at all, and instead have a much more silvery appearance.

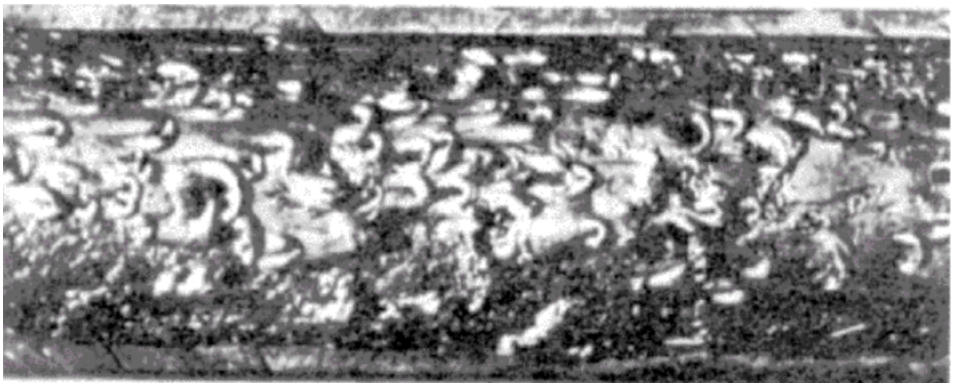

Figure 3: Typical impingement attack on Admiralty brass condenser tube. [2]

Dealloying, i.e. selective leaching, is a corrosion process in which the more electrochemically active metal is selectively removed from an alloy, leaving behind a porous weak deposit of the more noble metal. Specific categories of dealloying often carry the name of the dissolved element. So the preferential leaching of zinc from brass is called dezincification. Dezincification of the brass is caused by an insufficient content of arsenic as an alloying component which can prevent dezincification. In metallurgy, additions of arsenic or tin are necessary

to prevent this selective corrosion and dealloying occurs if the arsenic content is low. An example of an intensive dezincification process is shown in Figure 4. [7]

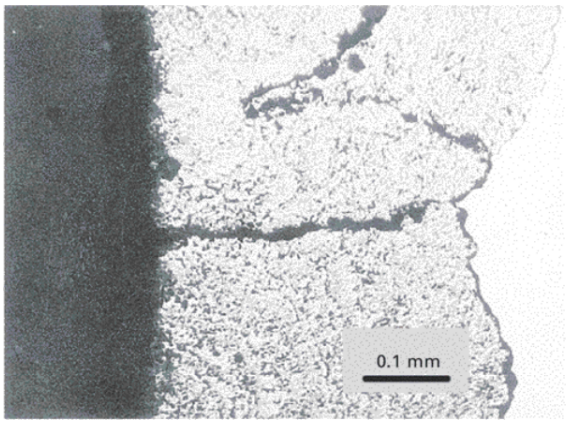

Figure 4: Metallographic cross-section through the wall of a pipe after 12 months of service in seawater. Dezincification of M70 alloy (Cu 69–71 %, rest Zn) reaches half of the wall thickness. [7]

Stress corrosion cracking or hydrogen induced cracking fracture is the growth of crack formation in a corrosive environment. It requires a specific corrosive environment and a simultaneous stress for it to occur. Several environments can cause SCC of copper and its alloys, of which the best known is ammonia (NH3) and its derivatives. The crack path in SCC is normally intergranular but transgranular could also occur in severely deformed metal [3]. Figure 5 [8] shows an example of a SCC image of brass in sulfate solution which contains ammonia ions.

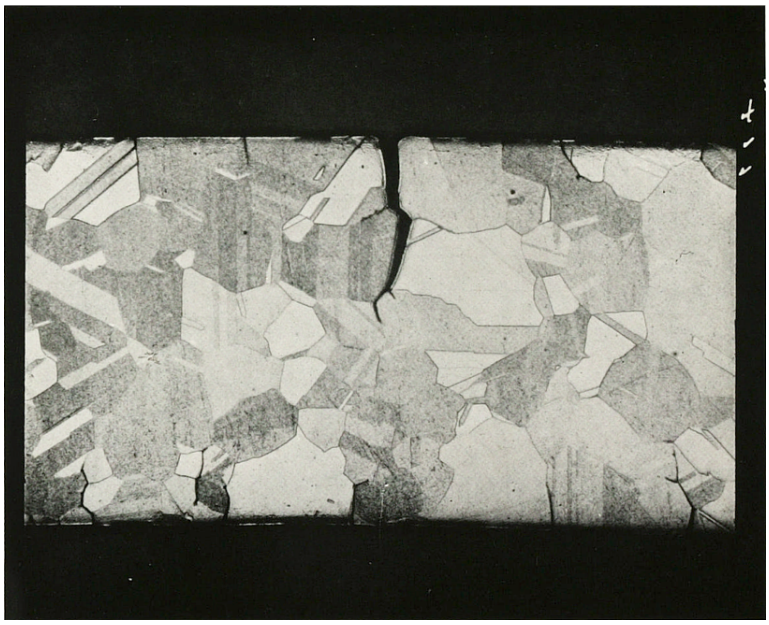

Figure 5: Photomicrograph of cracks in annealed 70 Cu 30 Zn brass, in sulphate solution which contains ammonia ions. [8]

1.3 Corrosion inhibitors

By now, some corrosion protection methods have been developed, e.g., coating, cathodic protection, anodic protection. Corrosion inhibitor is one of the effective protection methods.

The corrosion inhibitor defined by the National Association of Corrosion Engineers (NACE) is "a substance which retards corrosion when added to an environment in small concentrations." [9] According to the American Society for Testing and Materials' corrosion glossary, a corrosion inhibitor is defined as a chemical substance or combination of substances that, when present in the proper concentration and forms in the environment, prevents or reduces corrosion [1]. Besides, similar definitions such as "a chemical substance that decreases the corrosion rate when present in the corrosion system at suitable concentration, without significantly changing the concentration of any other corrosion agent" as defined by International Organization for Standardization (ISO) also exist.

Corrosion inhibition is reversible, and a minimum concentration of the inhibiting compound must be present to maintain the inhibiting surface film. Good circulation and the absence of any stagnant areas are necessary to maintain inhibitor concentration [1].

Inhibitors work in one or more ways to control corrosion, for example, by adsorption of a thin film onto the surface of a corroding material, by inducing the formation of a thick corrosion product or by changing the characteristics of the environment, leading to reduced aggressiveness. For instance, some inhibitors remove oxygen in the aqueous media to reduce the cathodic reaction. Although many chemicals can work as inhibitors, some of them are too expensive and not economically available. Chemicals that are toxic or not environmentally friendly are also of limited use. Moreover, inhibitors for one metal may or may not work for another or even may cause corrosion. Besides, the effectiveness of inhibitors also depends on the working environment such as the pH, temperature and water chemistry of the system. An example is that usually efficient inhibitors in acid solutions have little or no effect in near-neutral aqueous solutions.

As for an electrochemical corrosion process, the anodic process involves the electron-loss process of the metal material and the release of metal ions into the solution on the anode surface. On the other hand, the cathodic process consists of the absorption of an electron acceptor such as oxygen, hydrogen ions or oxides and the transfer of electrons from the electrode to an electron acceptor on the cathode surface. Besides, to construct an intact electric circuit, an ionic conductivity in the solution and an electronic conductivity in the metal are necessary. Corrosion inhibitors' functions are to minimize corrosion rates by stifling, retarding or completely stopping any or some steps of the corrosion process, that is [10]:

1. Decreasing the anodic or/and cathodic reaction. (The influence on the reaction process will subsequently affect the electrochemical behavior, Figure 6 illustrates the electrochemical result of inhibitors [11].)

   Anodic inhibitors reduce the actual rates of the metal dissolution that is the anodic reaction. Anodic or passivating inhibitors slow down corrosion by either stabilizing or repassivating the damaged passive film by forming insoluble compounds or by preventing adsorption of aggressive anions via competitive adsorption. They are used in the neutral pH range to treat cooling water systems, cooling system metals, and steel-concrete composites [1]. Chromate (CrO_4^{2-}) and nitrites (NO_2^-) are the best oxidizers that can passivate steel in deaerated solutions; however, both inhibitors have limited uses due to toxicity [12].

   Cathodic inhibitors are compounds that reduce the rates of the cathodic reactions, that is, the hydrogen evolution or oxygen reduction reactions. They may form precipitates in the cathodic locations to limit access to the cathodic reaction species, and they are also called precipitation inhibitors. For example, zinc salts are cathodic inhibitors that form precipitates of zinc hydroxide at the cathode [13], magnesium salts could work similarly [14]. Phosphate, as one of the most widely used corrosion inhibitors of steel, precipitates as ferrous and ferric phosphates on the metal surface [15]. However, in general, cathodic inhibitors are not very effective compared with anodic inhibitors (passivators).

   Mixed inhibitors are compounds that can retard the anodic and cathodic corrosion processes simultaneously by general adsorption covering the entire surface, sometimes with a polymer.

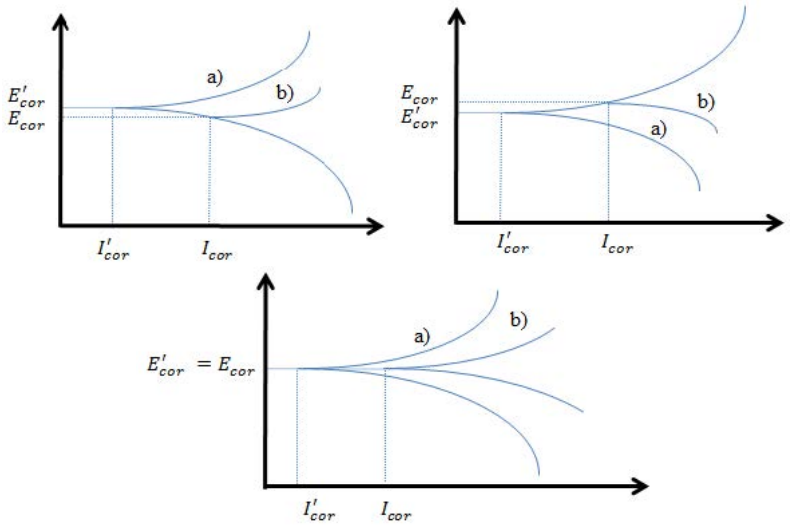

Figure 6: Theoretical potentiostatic polarization diagram: electrochemical behavior a metal on a solution containing a anodic (top left) or cathodic (top left) or both side (bottom) inhibitor (a) compared to the same solution without the inhibitor (b). [10]

2. Decreasing the diffusion rate of aggressive ions to the surface of the metal.

   Some aggressive ions, such as Cl^-, could accelerate the corrosion process, while inhibitors could retard their ionic diffusion rate to the metallic surface. For example, passivators increase stability of passive films, hence, they contribute in isolating the surface against aggressive ions.

3. Increasing electrical resistance of the metal surface by forming a film (coating) on it.

   The electrochemical corrosion involves a charge transfer process. Increasing the electrical resistance inhibits the charge transfer process.

Among these functions above, decreasing the reaction rate of the anodic reaction (with an anodic inhibitor) or the cathodic reaction (with a cathodic inhibitor) or both of them (with a mixed inhibitor) is the most important and effective one for most inhibitors.

Specific to organic compounds used as inhibitors, occasionally, they mainly act as cathodic inhibitors or anodic inhibitors or together, nevertheless, as a general rule, act through a process of surface adsorption, designated as a film-forming as shown in Figure 7 [11]. These inhibitors form a protective hydrophobic film by adsorbing molecules on the metal surface, which isolates the metal surface from the electrolyte. Due to their function mechanism, they must be soluble or dispersible in the medium surrounding the metal surface [16].

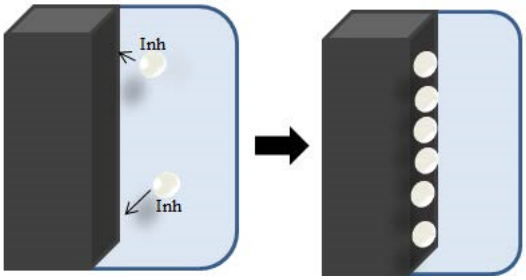

Figure 7: Illustration of the mechanism of actuation of the organic inhibitor: acting through adsorption of the inhibitor on the metal surface. Where the Inh represents the inhibitor molecules. [16]

According to some studies, the adsorption film barrier on the metal surface can be divided into two main types of interaction as follows [17]:

a Physisorption involves electrostatic forces between ionic charges or dipoles on the adsorbed species and the electric charge at metal/solution interface. In this case, the heat of adsorption is low and therefore this type of adsorption is stable only at relatively low temperatures.

b Chemisorption involves charge sharing or charge transfer from the inhibitor molecules to the metal surface to form a coordinate type bond. Electron transfer is typically for transition metals having vacant low-energy electron orbital. Chemisorption is characterized by much stronger adsorption energy than physical adsorption. Such a bond is, therefore, more stable at higher temperatures.

The chemisorption is characterized by a charge sharing or charge transfer process in the adsorption process. Many literatures indicate polar functional groups with S, O or N atoms in the molecule, heterocyclic compounds with π bonds, play important roles in chemisorption. S, O or N atoms are typical donor atoms that contribute to the adsorption and their inhibition efficiencies should follow the sequence O<N<S<P. For example, the nitrogen atom has the lonely sp_2 electron pair which is a potential electron provider [18]. Besides, some studies prove molecules that contain both nitrogen and sulfur in their structure are of particular importance since these provide an excellent inhibition in comparison with the compounds that contain only sulfur or nitrogen atoms [19]. For copper and copper alloys, due to the vacant d-orbitals of copper ions, coordinative bonds are easier to be formed by accepting electrons from inhibitor atoms. Therefore, donor atoms benefit the chemisorption of organic inhibitors. The most effective and efficient organic inhibitors are compounds that have π-orbitals. Unfortunately, they always present biological toxicity and environmental harmful characteristics [20, 21]. Donor atoms and π-orbitals are two main factors that can increase the chemisorption forming probability and strengthen the inhibition effect. The physicochemical properties which can affect the adsorption i.e. efficiency of the inhibitor molecule are listed below [18, 19, 22]:

Factors

1. chemical structure, such as the size of the organic molecule;
2. aromaticity and/or conjugated bonding, as the carbon chain length;
3. type and number of bonding atoms or groups in the molecule (either π or σ);
4. nature and the charges of the metal surface of adsorption mode like bonding strength to metal substrate;
5. ability for a layer to become compact or cross-linked;

6. capability to form a complex with the atom as a solid within the metal lattice;
7. type of the electrolyte solution like adequate solubility in the environment;

The study of adsorption processes of inhibitors on metallic surfaces is an important part of this master thesis.

1.4 Aims of the thesis

The objective of this thesis is to study the corrosion inhibition of copper alloys by organic compounds. For this objective, two groups of techniques were used. The first one is electrochemical techniques, it consists of Linear Polarization Resistance (LPR) measurements and Electrochemical Impedance Spectroscopy (EIS) analysis. Firstly, the corrosion resistance of Cu, Zn and 8 kinds of brass specimens under the protection of inhibitor, that is, 2-Mercaptobenzimidazole (MBI, the same below) or 1-Methyl-1H-benzimidazole-2-thiol (1H-HB-2T, the same below) were tested by Linear Polarization Resistance (LPR) measurements. Then, Cu, Zn and 50% Zn brass underwent Electrochemical Impedance Spectroscopy (EIS) analysis to understand the inhibition mechanisms. The second technique is the Fourier Transform Infrared spectroscopy (FTIR). Ex-situ and in-situ FTIR measurements were utilized to investigate adsorption processes and mechanisms of inhibitor molecules and metallic surfaces. It is noticeable that the key aim of this thesis is to understand the corrosion inhibition process and mechanisms of copper alloys by MBI and 1H-HB-2T rather than finding the most efficient inhibitor or the best corrosion-resistant alloy.

2 Experiments

This section introduces techniques and processes of experiments.

2.1 Experiment materials

There are 10 kinds of specimens available including pure copper, pure zinc and 8 kinds of brasses in this thesis. Brass alloys were supplied by the Technical University of Catalonia. Copper and brasses whose zinc content are below 50% are in the form of 4 mm thick sheet. For pure Zn samples, the plate thickness is 1 mm. For high zinc-bearing brasses samples, they are made by casting and are bullet-shaped. The information is shown in Table.2.

Table 2: Copper, zinc and brass samples.

Pure Cu	10% Zn	30% Zn	40% Zn	50% Zn	60% Zn	70% Zn	80% Zn	90% Zn	Pure Zn
4 mm thick plate				bullet-shaped					1 mm thick plate

For high zinc brass samples, on account of their non-cubic shape and high hardness, they were manually sawed into cylindric slabs of about 2 mm thickness and were soldered with rubber-cover copper wires on the back. Then they were embedded in epoxy resin. For plate samples, they can be easily cut by a disk cutting machine and if necessary they can be also soldered and embedded.

Two kinds of benzimidazole derivative compounds, 2-Mercaptobenzimidazole (MBI) and 1-Methyl-1H-benzimidazole-2-thiol (1H-HB-2T), were chosen. Their inhibition function has been reported by some literature [23, 24]. The basic physicochemical information of 2-Mercaptobenzimidazole is providen in Figure 8 and Table.3. Besides the structure shown below, S-BimH_2 has another different tautomeric form with the hydrogen atom moving from the sulfur atom to the nitrogen atom. Owing to its benzene ring structure and donor atoms (nitrogen atom and sulfur atom), it should have a good adsorption ability.

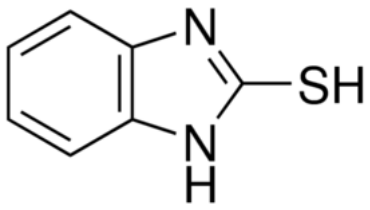

Figure 8: 2-Mercaptobenzimidazole (MBI) structure.

Table 3: MBI physicochemical information.

Empirical Formula (Hill Notation)	Molecular Weight ($g \cdot mol^{-1}$)	CAS Number	Solubility ($g \cdot L^{-1}$)
$C_7H_6N_2S$	150,20	583-39-1	0.3

The basic physicochemical information of 1-Methyl-1H-benzimidazole-2-thiol (1H-HB-2T) is providen in Figure 9 and Table.4. It has a similar structure with S-BimH_2 except the hydrogen atom on the nitrogen atom is substituted by a methyl functional group.

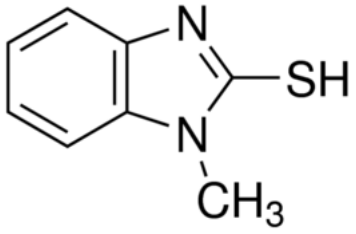

Figure 9: 1-Methyl-1H-benzimidazole-2-thiol (1H-HB-2T) structure.

Table 4: 1H-HB-2T physicochemical information.

Empirical Formula (Hill Notation)	Molecular Weight	CAS Number
$C_8H_8N_2S$	164.23	2360-22-7

It is noticeable that thione structure normally has a lower energy than thiol structure, so both MBI and 1H-HB-2T have the tendency to spontaneously transform from thiol to thione. Figure 10 provides two examples of thiol-thione transformation [23]. Similar transformation of 1H-HB-2T possibly happen as Figure 11 shows.

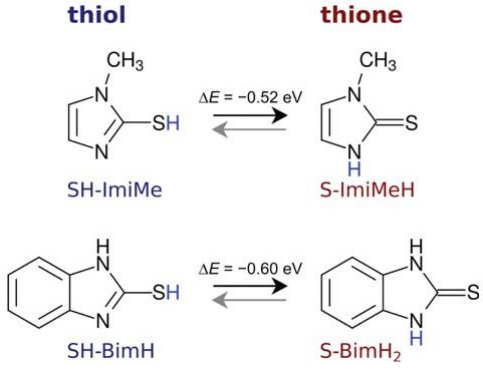

Figure 10: Examples of transformation from thiol to thione. [23]

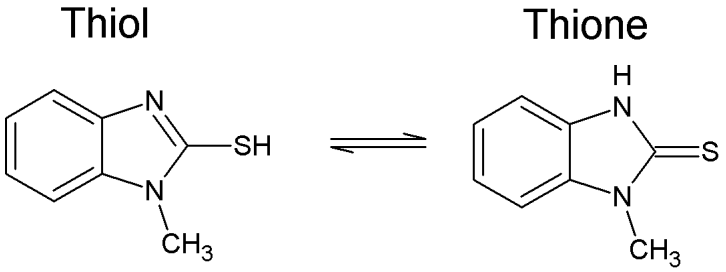

Figure 11: Possible transformation of 1H-HB-2T from thiol to thione.

Three kinds of solutions were prepared in electrochemical measurements, their constitutes were providen in Table.5. Solutions need to be mechanically stirred using a magnetic stirrer until complete dissolution is achieved. It should be noted that 1H-HB-2T is indissolvable only by stirring. An additional ultrasonic treatment with heating to 40 °C for 2 hours was applied to dissolve it.

Table 5: Electrolyte constitutes for electrochemical measurements.

Reference group	inhibitor group 1	inhibitor group 2
distilled water, NaCl 3%wt	distilled water, 3%wt NaCl and 1mM 2-Mercaptobenzimidazole (MBI)	distilled water, 3%wt NaCl and 1mM 1-Methyl-1H-benzimidazole-2-thiol (1H-HB-2T)

Two kinds of solutions for FTIR were made. 1 mM MBI and 1H-HB-2T solutions were prepared and the solvent is 99,8% pure Tetrahydrofuran (THF) rather than water.

2.2 Electrochemical measurements

Electrochemical measurements consist of Linear Polarization Resistance (LPR) and Electrochemical Impedance Spectroscopy (EIS).

2.2.1 Linear Polarization Resistance (LPR)

Linear Polarization Resistance (LPR) is one of the electrochemical polarization techniques. John Alfred Valentine Butler and Max Volmer established Butler-Volmer Model based on electrode kinetics and described the polarization by the current-overpotential equation:

$$j = j_0[\frac{C_O(0,t)}{C_O^*}e^{-\alpha_a \frac{nF}{RT}\eta} - \frac{C_R(0,t)}{C_R^*}e^{\alpha_c \frac{nF}{RT}\eta}] \quad (1)$$

If the solution is well stirred, or currents are kept so low that the surface concentrations do not differ appreciably from the bulk values, i.e. without Mass-Transfer limitation, the current-overpotential equation is further simplified to the Butler-Volmer equation [25]:

$$i = i_0[e^{-\alpha_a \frac{nF}{RT}\eta} - e^{\alpha_c \frac{nF}{RT}\eta}] \tag{2}$$

i electrode current density, A/m^2 (defined as j = I/S)

i_0 exchange current density, A/m^2

T absolute temperature, K

z number of electrons involved in the electrode reaction

F Faraday constant

R universal gas constant

$C_O(0,t)$ the time-dependent concentration of the species to be oxidized at the distance zero from the surface

$C_R(0,t)$ the time-dependent concentration of the species to be reduced at the distance zero from the surface

C_O^* the bulk concentration of the species to be oxidized, mol/cm^3

C_R^* the bulk concentration of the species to be reduced, mol/cm^3

α so-called anodic charge transfer coefficient, dimensionless

β so-called cathodic charge transfer coefficient, dimensionless

η activation overpotential (defined as $\eta = E - E_{eq}$)

Sometimes $\frac{nF}{RT}$ is replaced by the sign of f.

By a series of mathematical simplifications, the current-overpotential equation when the potential is far from the corrosion potential, E_{corr} and both anodic and cathodic reactions are controlled by charge transfer can be expressed by anodic Tafel slope β_a and cathodic Tafel slope β_c. Then Stern-Geary equation [26], i.e. Equation.3, can be obtained [27]. R_p is the polarization resistance. Based on the inverse proportional relationship between i_0 and R_p, Linear Polarization Resistance measurement provides the polarization resistance which can be used to estimate the self corrosion current and the corrosion rate..

$$R_p \approx \frac{1}{i_0}\frac{\beta_a\beta_c}{2.3(\beta_a+\beta_c)} = \frac{\Delta E}{\Delta i_{\Delta E \to 0}} \tag{3}$$

A typical LPR measurement result is shown below [28]. By using built-in fitting tools of EC-Lab such as R_p fit or Linear fit, corresponding linear polarization resistance can be calculated.

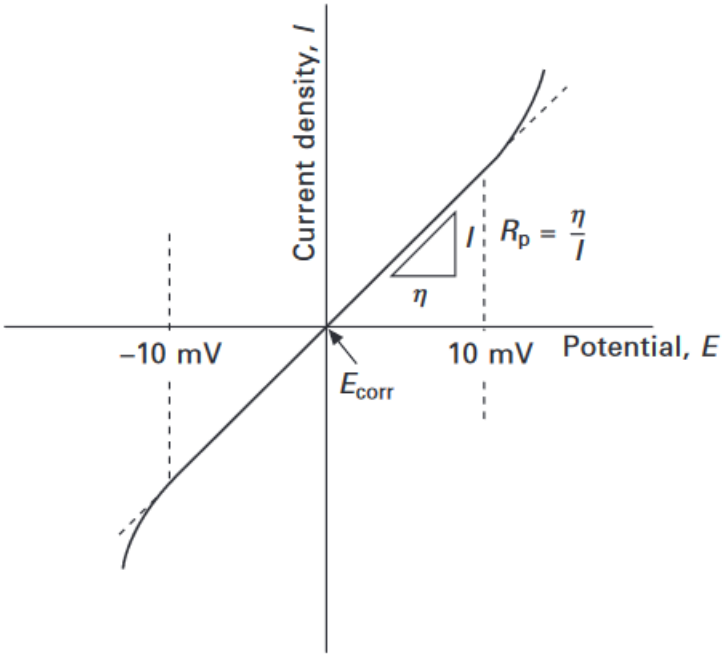

Figure 12: Schematic of the LPR fitting. [28]

For the inhibitor investigation, an index calculated from LPR could be used to show inhibitors' protection effects. It is the inhibition efficiency η (%) of a corrosion inhibitor on the tested specimen surface in a certain aggressive environment. The Equation.4 provides the inhibition efficiency.

$$\eta = \frac{i_O - i'_O}{i_O} \times 100\% = \frac{R'_p - R_p}{R'_p} \times 100\% \tag{4}$$

i_O the corrosion current density without the inhibitor addition

i'_O the inhibited corrosion current density

R_p the polarization resistance without the inhibitor addition

R'_p the inhibited polarization resistance

All the 10 kinds of specimens for electrochemical tests were ground mechanically with different grades of silicon carbide paper (from 320 to 4000) followed by wet polishing, that is, using MD Mol cloth in combination with 3 um slurry, then MD Nap cloth with 1 um

slurry. Samples were then cleaned with ethanol in an ultrasonic bath for 10 min, rinsed with ethanol and distilled water and finally dried with nitrogen gas. After polishing and cleaning, a piece of copper tape was glued on the back of the plate sample to guarantee the next electrical connection between the electrochemical workstation and the sample (this step is only for non-embedded plate samples, it can be omitted for embedded samples). Then the sample is wrapped with solution-resistant epoxy-tape leaving unprotected a defined circular area (which is normally chosen 0.8 cm diameter, i.e. 0.50264 cm^2) and an example is shown in Figure 13. One problem is that sometimes the crevice corrosion was serious and water could permeate the covered area from the tape edge especially when it comes to active specimens such as zinc. The only solution is to clean the metal surface thoroughly and paste the tape tightly.

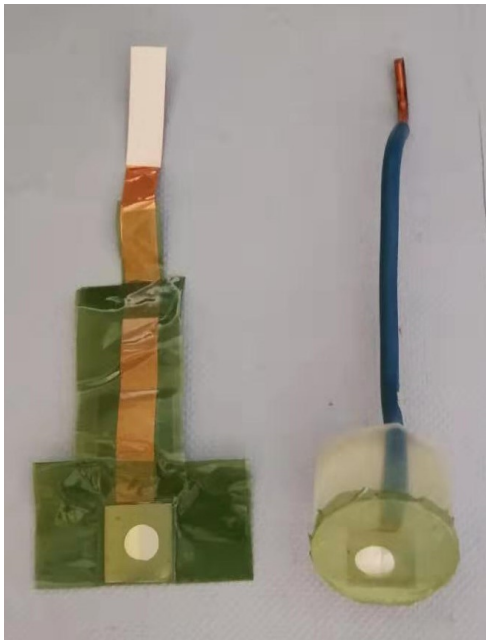

Figure 13: Sample configurations used for LPR measurements.

The electrochemical workstation is VSP-300 of Bio-Logic Science Instruments and a three-electrode system was used for LPR measurements. The working electrode was the tested sample. Saturated Calomel Electrode (SCE) and a graphite electrode were used as the reference electrode and the counter electrode respectively. Corresponding placements and connections are shown below.

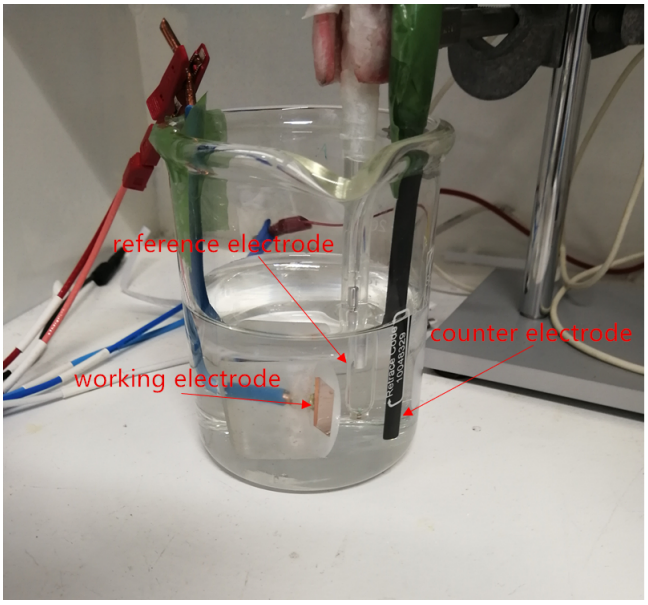

Figure 14: The three-electrode cell system.

According to the use principle of LPR and previous experience, the potential was applied at a small range of ± 5 mV against E_{corr} with the scanning rate 0.1 mv/s. The parameters of LPR experiment was set up as Figure 15 shows. And the LPR measurement time for each specimen is providen in Table.6.

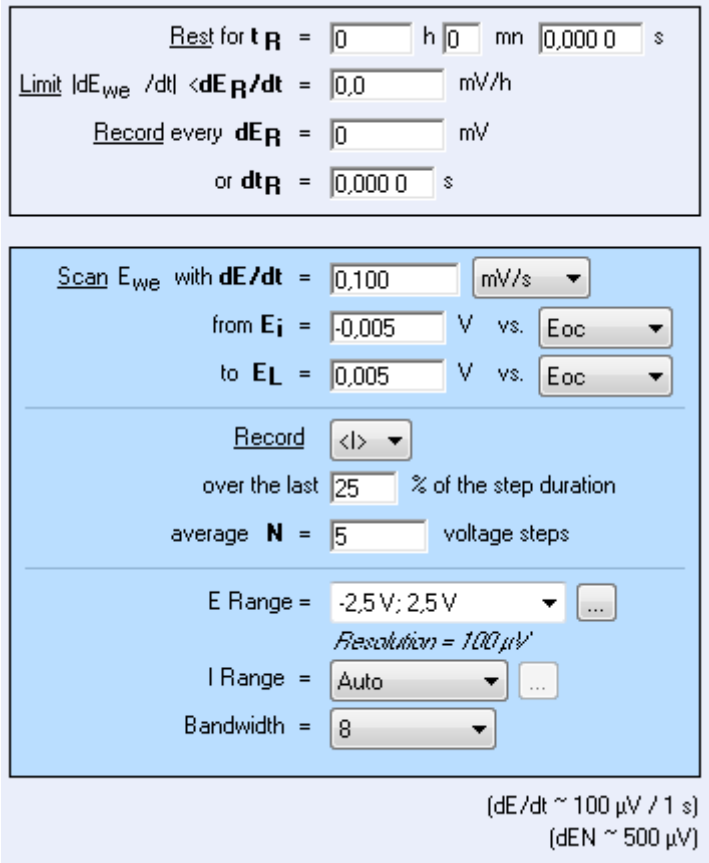

Figure 15: LPR software setup.

Table 6: LPR measurement time after the start of each experiment.

Measurement time (hours)	2	5	10	20	30	40	50	60	70	80	90	100

After adding 100 ml inhibitor or reference solution in the cell and starting the electrochemical workstation, the LPR measurement starts.

2.2.2 Electrochemical Impedance Spectroscopy (EIS)

Electrochemical Impedance Spectroscopy (EIS) is widely used for the characterization of electrode processes and complex interfaces. Electrochemical impedance normally applies a small amplitude AC potential signal to an electrochemical cell and studies the feedback AC signal of the system. Most commonly, EIS can be measured using a "single-sine" method where individual frequencies are measured sequentially or a multisine implementation which measures all frequencies at one time but needs Fourier transform later [29]. Analysis of the system response contains information about the interface. Based on the EIS data, the mathematical model and equivalent circuit model can be established. Then its structure and reactions taking place on the surface can be obtained.

Electrochemical impedance is normally measured using a small excitation signal to make the cell's response pseudo-linear. In a linear or pseudo-linear system, the current response to a sinusoidal potential will be a sinusoid at the same frequency but shifted in phase (see Figure 16 [30]). And corresponding mathematical expressions are listed below:

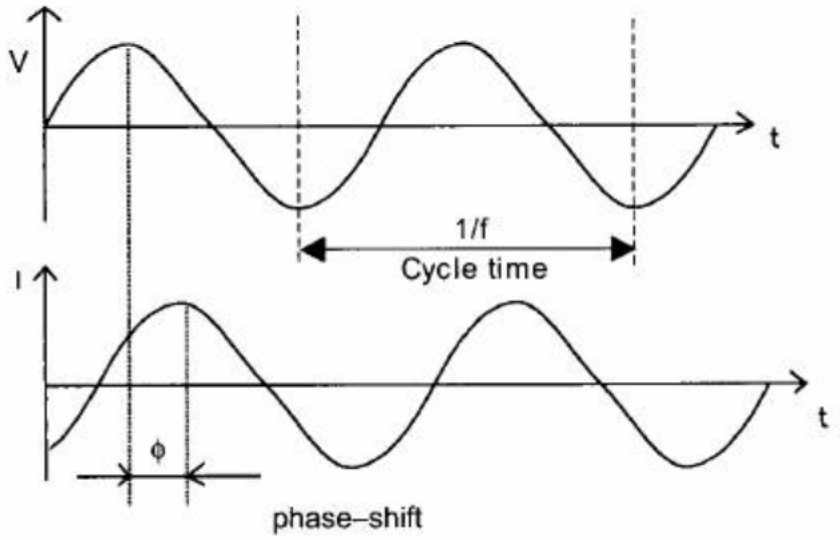

Figure 16: Sinusoidal current response in a Linear System. [30]

$$\omega = 2\pi f \tag{5}$$

$$V_t = V_0 sin(\omega t) \tag{6}$$

$$I_t = I_0 sin(\omega t + \phi) \tag{7}$$

With Eulers relationship,

$$exp(j\phi) = cos(\phi) + jsin(\phi) \tag{8}$$

If the V_t and I_t are both described by natural exponent, the below equation form can be obtained,

$$Z_\omega = \frac{V}{I} = Z_0 exp(j\phi) = Z_0(cos(\phi) + jsin(\phi)) \tag{9}$$

V_t the input voltage, V

V_0 the voltage amplitude, V

I_t the output measured current

I_0 the current amplitude, A

ω angular frequency, rad/s

ϕ phase Angle, rad

Z_ω the impedance represented as a complex number

From the Equation.9, the expression for Z_ω is composed of a real and an imaginary part. If the real part is plotted on the X-axis and the imaginary part is plotted on the Y-axis of a chart, a Nyquist plot is obtained. An alternative representation is a Bode plot in which log |Z| and ϕ are both plotted against log frequency. The circuit structure [30], Nyquist plot and Bode plots of a parallel RC equivalent electronic circuit are providen below [25].

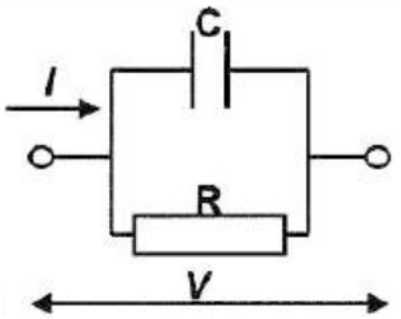

Figure 17: The parallel RC circuit structure. [25]

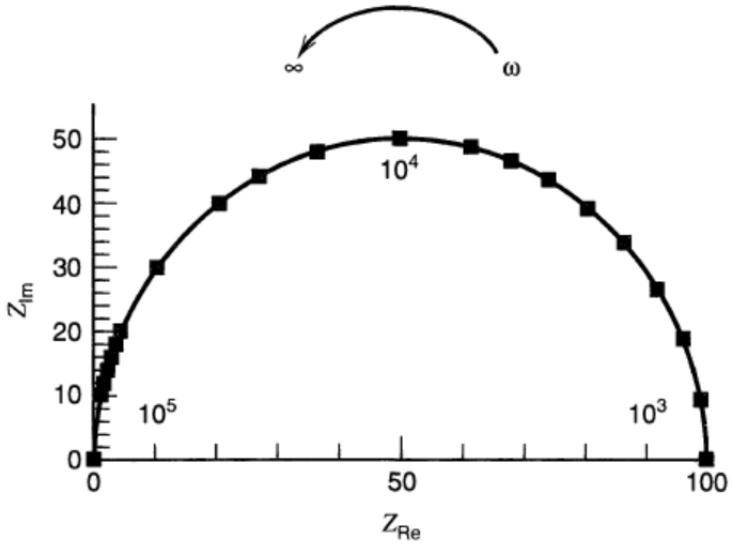

Figure 18: Nyquist plot for a parallel RC circuit with R = 100 Ω and C = 1 μF. [25]

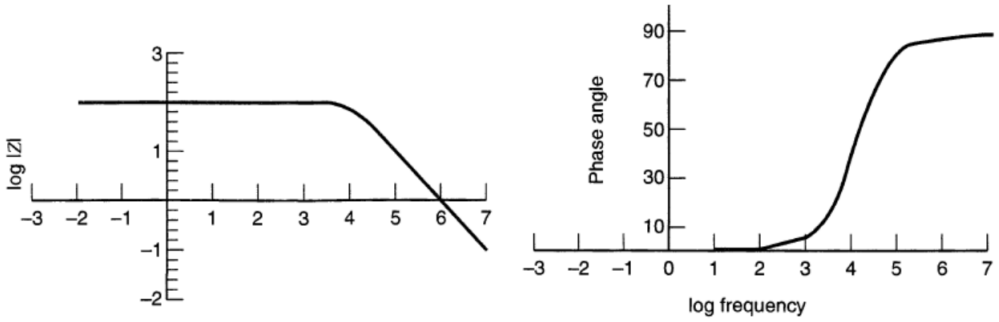

Figure 19: Bode plots for a parallel RC circuit with R = 100 Ω and C = 1 μF. [25]

After all these 10 kinds of specimens were measured by LPR, 3 kinds of specimens which are of specific research value were investigated by EIS. In the experiments, regardless of whether samples are platelike or cylindrical, they were embedded in resin before grinding and polishing. Then the optical microscope and corresponding area measurement software were utilized to measure its bare metallic surface. Once the area of each specimen was measured, they can be ground, polished and cleaned as same as the steps in LPR and one example is providen in Figure 20. This method also has a crevice corrosion problem but compared with that in LPR measurements, it is negligible.

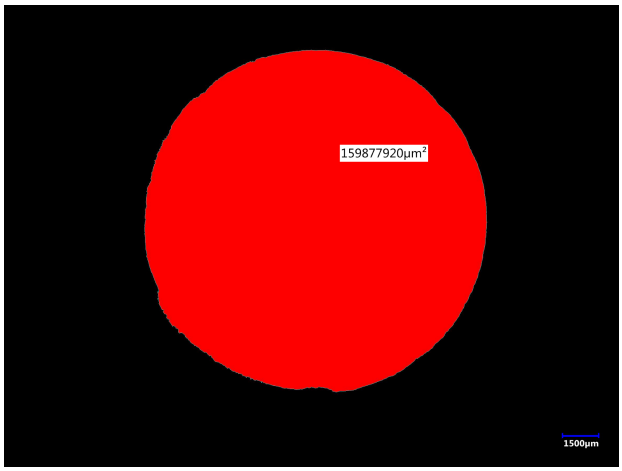

(a) The measured area by optical microscope software

(b) Real image of the sample

Figure 20: Sample configuration of EIS measurements

The electrochemical workstation VSP-300 of Bio-Logic Science Instruments and a three-electrode system were used. The working electrode was the tested sample. Saturated Calomel Electrode (SCE) and a graphite electrode were used as the reference electrode and the counter electrode respectively. Corresponding placements and connections were done as the same as that in LPR measurements. The measurement time arrangement is listed in Table.7. The frequency range used for the EIS was: 100kHz – 0,01Hz with an AC amplitude of 10 mV, 10 steps/decade. The perturbation was applied with respect to the OCP. The detailed setup is shown in Figure 21.

Table 7: EIS measurement time after the start of each experiment.

Measurement time (hours)	2	5	10	20	30	40	50

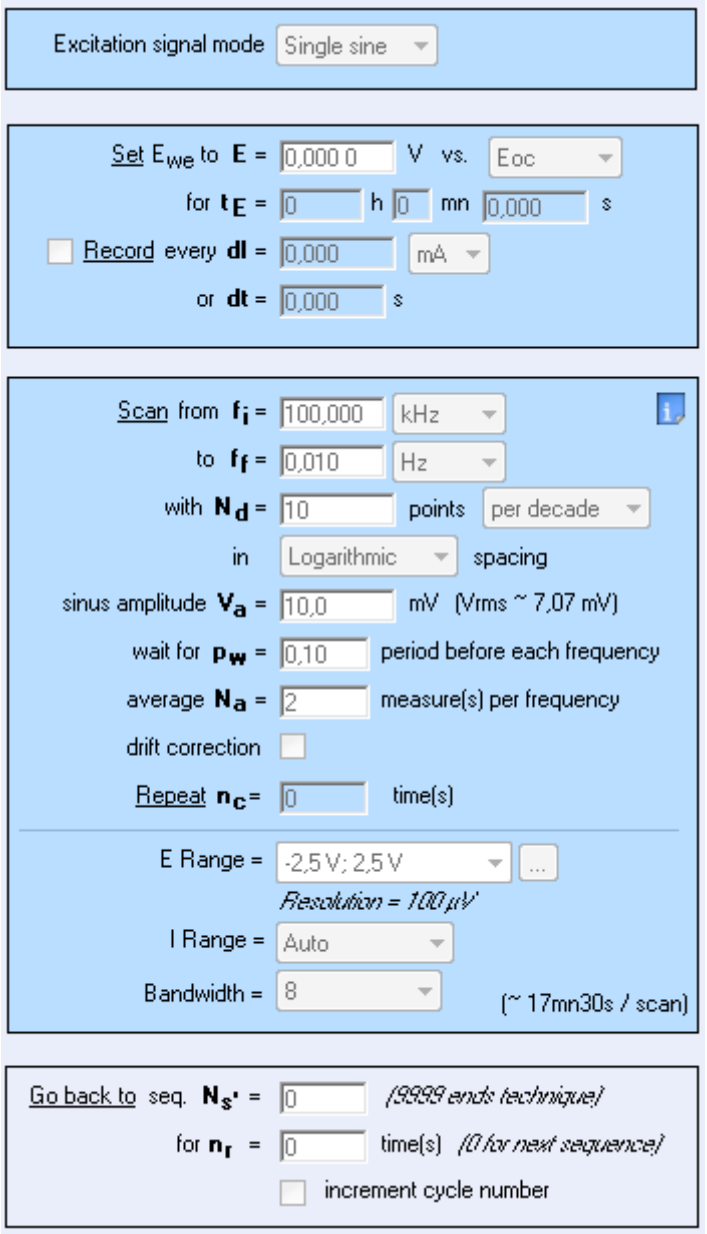

Figure 21: EIS software setup.

After adding 100 ml inhibitor or reference solution in the cell and starting the electrochemical workstation, the EIS measurement could start.

2.3 Fourier Transform Infrared Spectroscopy(FTIR)

Fourier Transform Infrared Spectroscopy(FTIR) was applied to investigate inhibitors' adsorption mechanisms on the surface in this section.

Fourier Transform Infrared Spectroscopy (FTIR) indicates the Fourier Transform mathematical treatment of infrared spectral data [31]. It is a useful tool for identifying types of chemical bonds in a molecule by producing an infrared absorption or emission spectrum that is like a molecular "fingerprint". The general configuration of an FTIR imaging microspectrometer is shown in Figure 22 [32]. As introduced in the above part, the inhibition effect of organic inhibitors directly depends on some specific atoms and functional groups, so with the help of FTIR, organic inhibitors' functional mechanisms can be deduced.

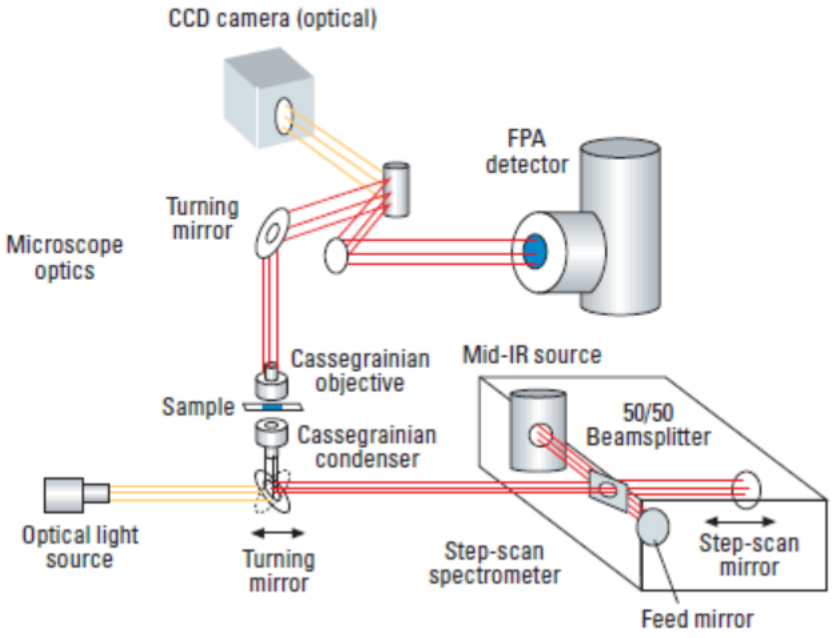

Figure 22: Schematic of a typical FTIR imaging spectrometer. [32]

When a beam of continuous wavelength infrared light irradiates on one kind of molecule, if the vibration frequency or the rotational frequency of a chemical bond of the molecule, this kind of molecule will absorb infrared radiation and jump from the ground vibration or rotation energy level to the higher vibration or rotation energy level. Based on the vibration or rotation information, chemical bonds are measured and the existence of corresponding atoms or functional groups in the molecules can be proved. Among different infrared spectral wavelengths, the mid-infrared region (wavenumber: 4000-400 cm^{-1}) is the most widely used one since it corresponds to the fundamental frequency of the chemical bonds' vibration. And FTIR normally indicates the infrared absorption spectrum in the mid-infrared region.

FTIR also has its conditions of application:

1. The frequency of vibration or rotation in the functional group matches one of frequen-

cies of incident infrared radiation and this frequency is called the characteristic frequency

2. The dipole moments of the measured functional groups need to change during their vibrations. In other words, if the dipole moment of a functional group does not change, it has no infrared vibration absorption

Since different functional groups may have absorption at the same frequency and the characteristic vibration frequencies of functional groups change (red shift and blue shift) with different chemical environments, the analysis of a spectrum is much more complex than directly identify functional groups from some specific frequencies. Besides, the fringing effect of FTIR also increases the difficulty of analyzing FTIR spectra. It indicates meaningless strong interference fringes which hinder the spectra reading by covering the original peaks. These fringes always appear as the form of quasi-sinusoidal shape superimposed on the real spectrum. It is caused by interferences of IR beams reflected on the film surface and the film-substrates interface or by interferences of multiple beams reflected on the substrate. [33, 34, 35]

A typical fringe pattern from our FTIR experimental result is shown in Figure 23. Fringes in FTIR is almost inevitable, the wisest way to do is to avoid these fringing districts during analysis.

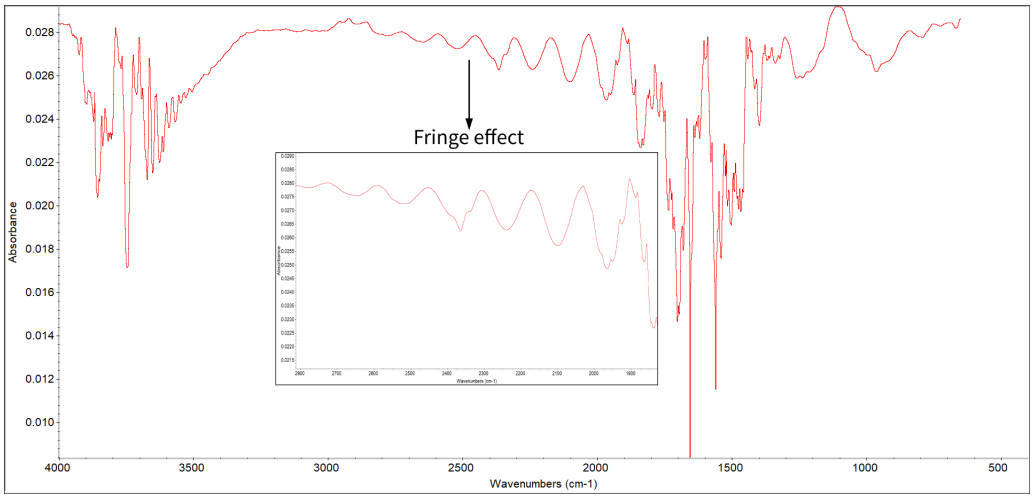

Figure 23: A fringing example in FTIR.

Vibrational spectroscopy by FTIR instruments is successfully applied to such films deposited on a flat metal substrate using reflection-absorption spectroscopy (RAS) and attenuated total

reflectance (ATR). Reflection-absorption implies the reflected infrared spectrum after the absorption process on the surface of the substrate is analyzed. For adsorbates on a metallic or conducting film, absorption of IR radiation by the adsorbate overlayer was enhanced at high angles of incidence (near grazing) and involved only one polarization of the incident IR beam. Attenuated total reflectance IR spectroscopy combines IR spectroscopy with total internal reflection to restrict the analysis volume. The IR spectrum is obtained from the substrate in contact with the ATR crystal which is made of selenide or germanium. The ATR and RAS provide a quasi-absorption spectrum which is not identical but is similar to a transmission spectrum, the interpretation of results may be much easier than in the case for other reflection techniques, which provide dispersive spectra. [36, 37, 38]

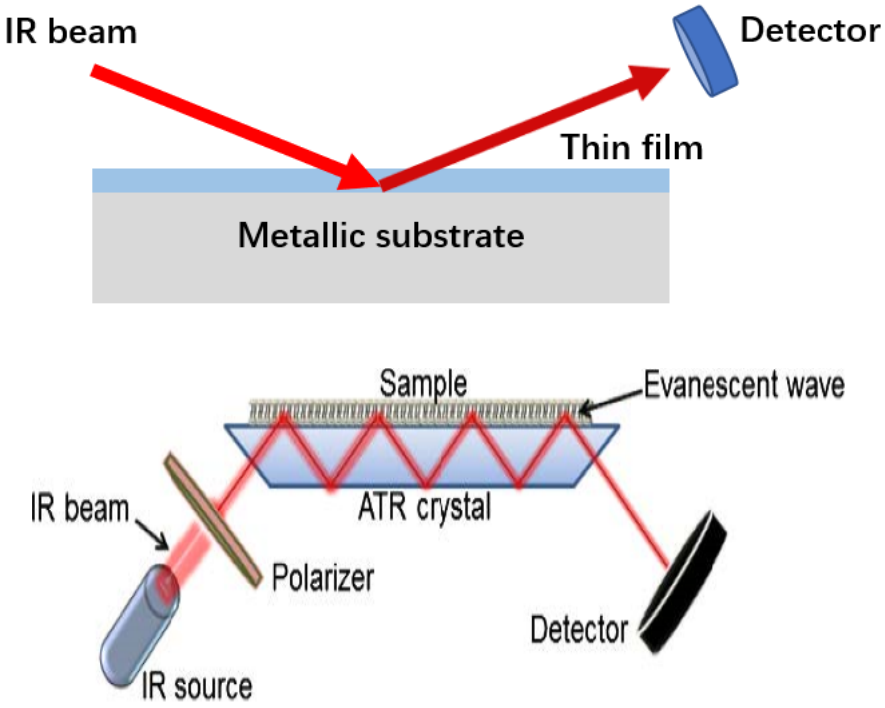

Figure 24: Optical configurations of surface-sensitive infrared techniques. (top): RAS, (bottom): ATR

In this part, ex-situ FTIR measurements adopted the reflection-absorption spectroscopy (RAS) and in-situ adopted attenuated total reflectance (ATR). FTIR measurement was performed on samples using NICOLET 6700 FT-IR spectrometer from Thermo Electron Corporation. This machine provides multiple smart accessories. were utilized for each kind of experiment. Its detailed introduction is providen by its operation brochure and Thermo website.

Figure 25: The NICOLET 6700 FTIR machine.

2.3.1 Ex-situ FTIR

After previous electrochemical measurements, research emphasis gradually shrank to the Cu, 50% Zn brass and Zn. In the ex-situ FTIR part, Cu, 50% Zn brass and Zn were ground, polished and cleaned as the same as the work in electrochemical measurements. Before the actual test, the background spectra of the metal surfaces were recorded. Then these specimens were immersed in 20 ml 1 mM MBI or 1H-HB-2T THF solution for 30 minutes. After the exposure, the specimens were rinsed in pure THF for 5 seconds and dried by N_2 gas flux. Finally, the polished smooth surfaces were placed towards the hole of the FTIR accessory and tested one by one. The measured wavenumber region was at the range of 4000 cm^{-1} to 400 cm^{-1}.

2.3.2 In-situ FTIR

In in-situ FTIR measurements, firstly Physical Vapor Deposition (PVD) machine has been used to deposit a thin copper film or a thin zinc film on the ATR crystal (germanium). Because PVD cannot produce eligible 50% Zn brass thin film, only Cu and Zn were studied in this part. Before the deposition, the Ge crystal was rinsed in acetone and ultrasonically cleaned in ethanol for 5 min to remove impurities on the surface. Then it was immersed in Milli-Q water (MQ water) with ultrasonic clean for 5 min and rinsed by MQ water and dried.

The metal film thickness on the ATR crystal surface is important. A high thickness film cannot be penetrated by the incident infrared light, so the information at the specimen/solution

interface cannot be detected. If the thickness is not thick enough, due to the phenomenon observed in experiments that the metal film will be dissolved during in-situ experiments, it cannot sustain enough long experimental period. Based on experiences, the thickness of the deposited films on the Ge crystal was defined at about 50 nm. On the other hand, to ensure the integrity and homogeneous thickness of films, the deposition rate should be set as low as possible, that is, at around 0.2-0.4 Å/s. The PVD machine used here is Rack Type Vacuum Evaporator VCM 600-SP3. Detailed parameter setup and deposition procedures are detailly introduced in the machine operation brochure.

After the PVD preparation, the accessory configuration was done as shown in 26. Then the background spectra collection was conducted by collecting the spectra of the sample exposed to pure THF. Finally, the pure THF was replaced by 1 mM MBI or 1H-HB-2T THF solution and the experiment began. The measured wavenumber region was at the range of 4000 cm^{-1} to 400 cm^{-1}.

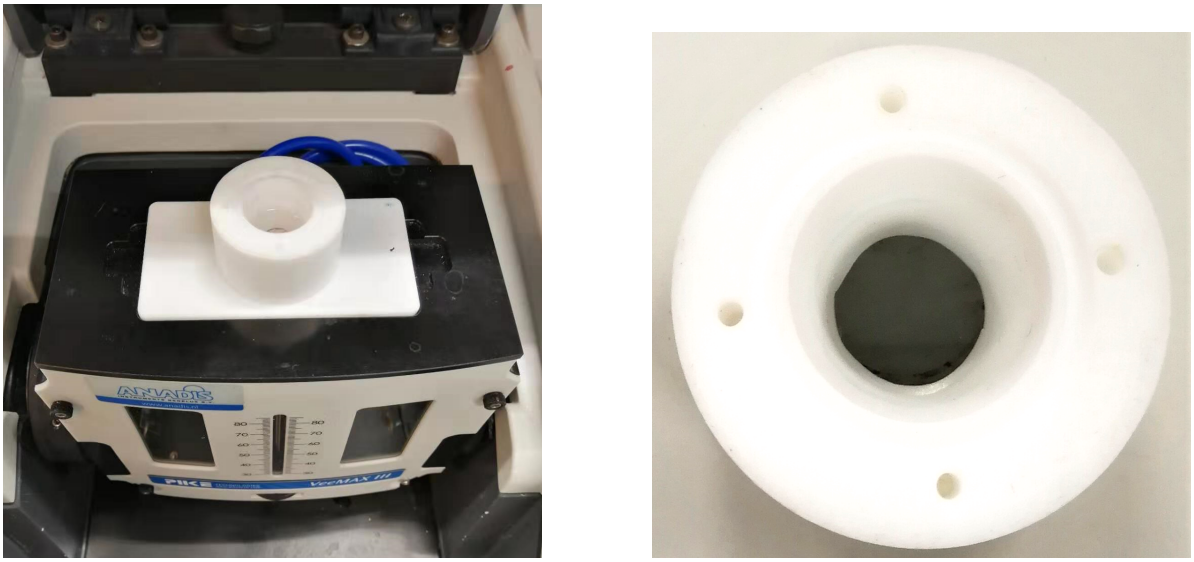

(a)lateral view (b)vertical view

Figure 26: The configuration of in-situ FTIR accessory.

3 Results and discussion

10 kinds of metallic specimens and 2 organic corrosion inhibitors were studied in this thesis. Initially, LPR measurement was used to compare the inhibition performances of specimens. Subsequently, 3 kinds of specimens of research value were chosen. Repetitive LPR measurements over these specimens were done to calculate the average results and guarantee reliability. Then EIS tests were conducted to investigate the corrosion process. Finally, both ex-situ and in-situ FTIR were used to study the adsorption of inhibitor molecules on metallic surfaces.

3.1 Electrochemical measurements

Electrochemical measurements are used to investigate the corrosion performance of each specimen. The corrosion reactions for Cu, Zn, and brass substrates in aerated chloride solutions are described as follows.

The cathodic reaction of Cu in NaCl solution is the reduction of oxygen. The anodic reaction product CuCl, which is only slightly soluble in dilute sodium chloride, reacts to produce Cu_2O. With the increase of immersion, other products such as $Cu(OH)_2$ or CuO, and $Cu_2(OH)_3Cl$ or $CuCO_3 \cdot Cu(OH)_2$ are formed in chloride solution [39].

Cathodic reaction of Cu in NaCl solution,

$$O_2 + 2\,H_2O + 4\,e^- \longrightarrow 4\,OH^-$$

Anodic reaction of Cu in NaCl solution,

$$Cu + 2\,Cl^- \longrightarrow CuCl_2{}^- + e^-$$
$$Cu + 2\,Cl^- \longrightarrow CuCl_2 + 2\,e^-$$

The cathodic reaction of Zn in NaCl solution is the reduction of oxygen or the generation of hydrogen. The main anodic reaction products of Zn are $Zn(OH)_2$ and $ZnCl_2$.

Cathodic reaction of Cu in NaCl solution,

$$O_2 + 2\,H_2O + 4\,e^- \longrightarrow 4\,OH^-$$
$$2\,H_2O + 2\,e^- \longrightarrow 2\,OH^- + H_2\uparrow$$

Anodic reaction of Cu in NaCl solution,

$$\mathrm{Zn} \longrightarrow \mathrm{Zn}^{2+} + 2\,\mathrm{e}^{-}$$
$$\mathrm{Zn} + 2\,\mathrm{OH}^{-} \longrightarrow \mathrm{Zn}^{(}\mathrm{OH})_2 \downarrow + 2\,\mathrm{e}^{-}$$

The corrosion reactions for brasses are complex. All reactions of Cu and Zn can be found in the brass corrosion process. Besides, Cu ions can be reduced by Zn metal and such reduction reactions lead to the increased formation of soluble zinc complexes and precipitation of Cu within the pores of the CuCl layer [40].

Reduction reactions of cupric ion by zinc in NaCl solution,

$$2\,\mathrm{CuCl_2}^{-} + \mathrm{Zn} \longrightarrow 2\,\mathrm{Cu} + \mathrm{ZnCl_4}^{2-}$$
$$\mathrm{Cu_2O} + \mathrm{Zn} + 2\,\mathrm{Cl}^{-} + \mathrm{H_2O} \longrightarrow 2\,\mathrm{Cu} + \mathrm{Zn(OH)_2Cl_2}^{2-}$$

Reduction reaction of cuprous ion by zinc in NaCl solution,

$$\mathrm{CuO} + \mathrm{Zn} + 2\,\mathrm{Cl}^{-} + \mathrm{H_2O} \longrightarrow \mathrm{Cu} + \mathrm{Zn(OH)_2Cl_2}^{2-}$$

Due to the existence of organic inhibitors, the situation could be even more complex. For example, Figure 27 and 28 provde two possible structures of Cu^{2+} complexes in the MBI solution. Similar complexes can be considered also for the 1H-HB-2T molecules. Thus, a compound film which consists of metallic oxides and organic inhibitor molecules will form on the metal surface. On the one hand, the formation of this mixed copper–zinc oxide polymer surface film represents an effective barrier against corrosion of both metal components in the Cu-based alloys in chloride solution. Such a complex layer will increase the difficulty of the analysis of electrochemical experiment results. During the electrochemical experiments, a visible white layer was formed on the surface of high zinc brasses and pure Zn instead of Cu in all three kinds of solutions. The basis of the white layer is most likely to be $Zn(OH)_2$. This is because $Zn(OH)_2$ is slightly soluble at room temperature in neutral water and such a white layer was only observed in high zinc content metals. Figure 29 shows the metallic surfaces after corrosion in 1H-HB-2T solution. Similar results are observed in MBI and reference solutions.

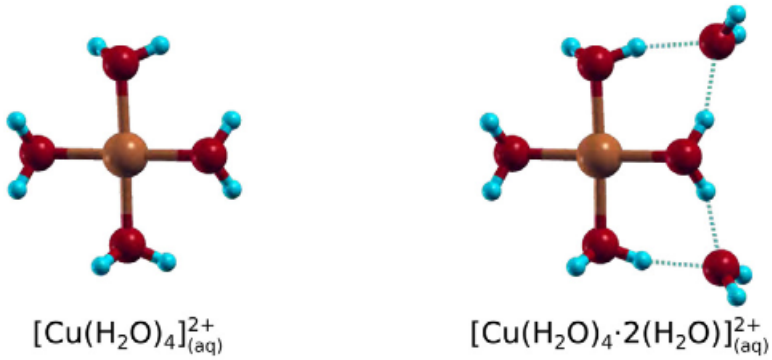

Figure 27: Two simple models of hydrated Cu^{2+} ion, i.e., $[Cu(H_2O)_4]^{2+}_{(aq)}$ and $[Cu(H_2O)_4 \cdot 2(H_2O)]^{2+}_{(aq)}$. [41]

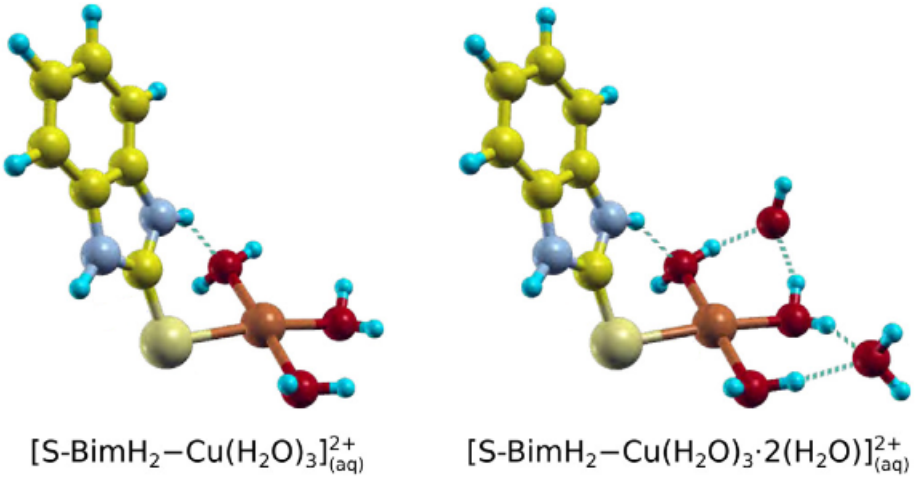

Figure 28: Models of MBI forming a complex with hydrated Cu^{2+} ion, i.e., $[MBI\text{-}Cu(H_2O)_3]^{2+}_{(aq)}$ and $[MBI\text{-}Cu(H_2O)_3 \cdot 2(H_2O)]^{2+}_{(aq)}$. [41]

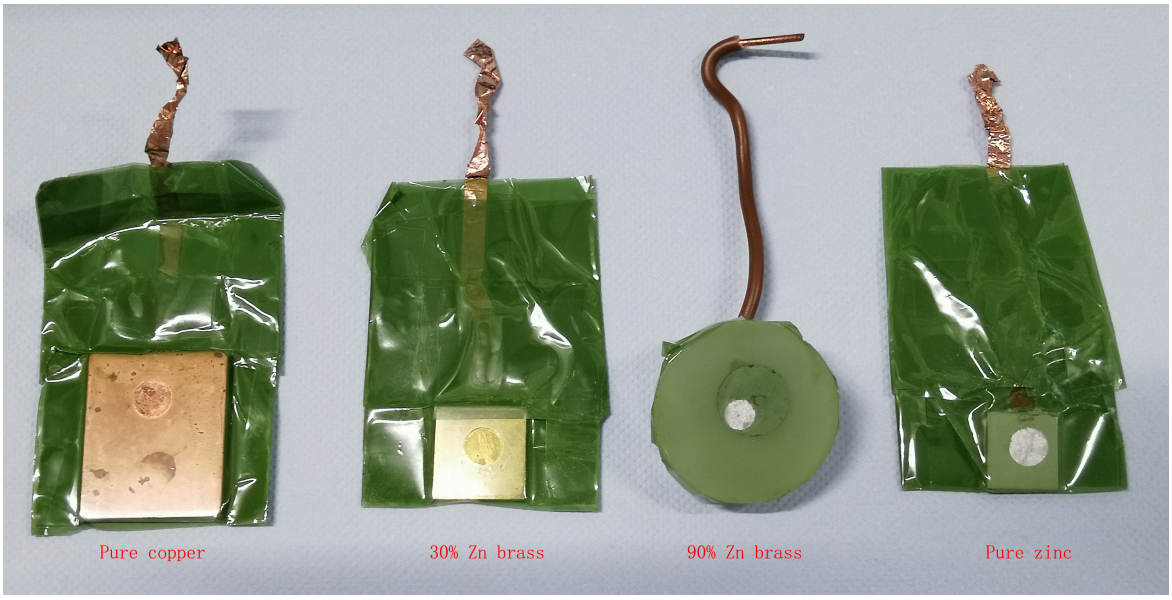

Figure 29: Surface appearance after corrosion in the 1H-HB-2T solution.

3.1.1 Linear Polarization Resistance (LPR)

3.1.1.1 Specimens in 1 mmol/L MBI solution

Figure 30 shows the polarization resistances of specimens in 1 mM MBI solution (which also contains 3%wt. NaCl and distilled water). In the view of metallic type, copper and alpha brasses whose zinc content is below 40% have high polarization resistances and the polarization resistances of specimens decreased with the increase of Zn content generally. The only exception is 60% Zn brass of Gamma phase which has a relatively high polarization resistance. Although there are some fluctuations by the exposure time, the general trend for copper, alpha brasses and 60% Zn brass is that polarization resistances rise firstly and then decrease. The first increase could be explained by the adsorption process of inhibitor molecules onto the oxide-covered surface and/or its incorporation into the oxide film. The latter decrease is likely to be caused by the desorption of inhibitor molecules.

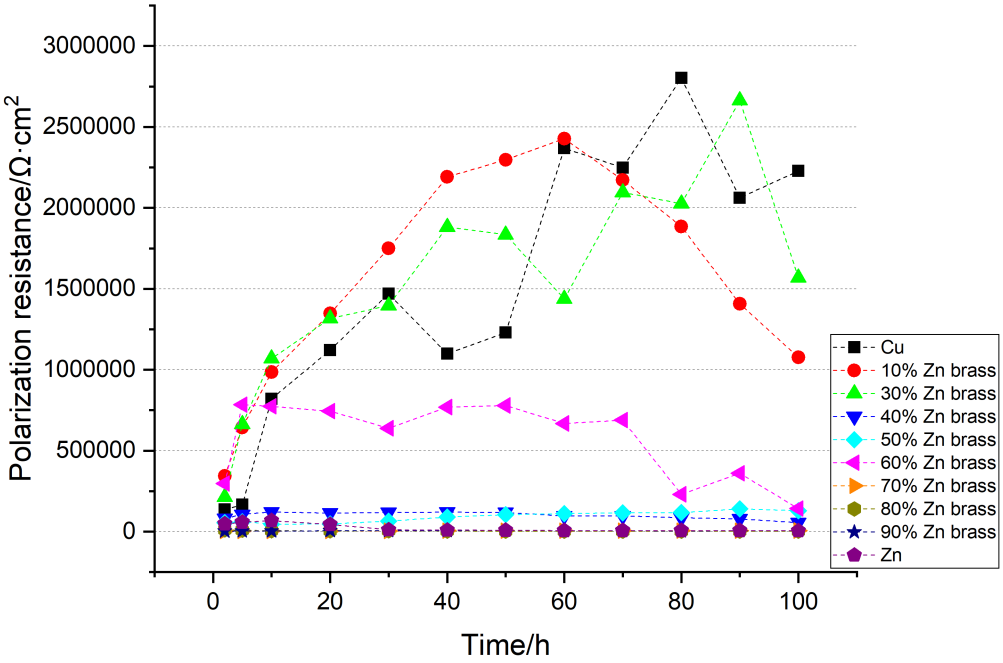

Figure 30: Polarization resistance values of specimens immersed in 100ml 1 mM MBI solution.

According to Equation.4, inhibition efficiencies of MBI are calculated and divided into 2 groups: group 1 and group 2. group 1 includes copper, 10% Zn brass, 30% Zn brass, 40% Zn brass, 60% Zn brass, zinc while group 2 consists of 50% Zn brass, 70% Zn brass, 80% Zn brass, 90% Zn brass. The results are shown in Figure 31 and 32. This group division bases on the inhibition efficiency.

In group 1, MBI maintain high inhibition efficiencies which are more than 97% for copper, 10% Zn brass, 30% Zn brass during the whole experiment period while the efficiencies for 40% Zn brass, 60% Zn brass and zinc decrease gradually from around 98% at the beginning.

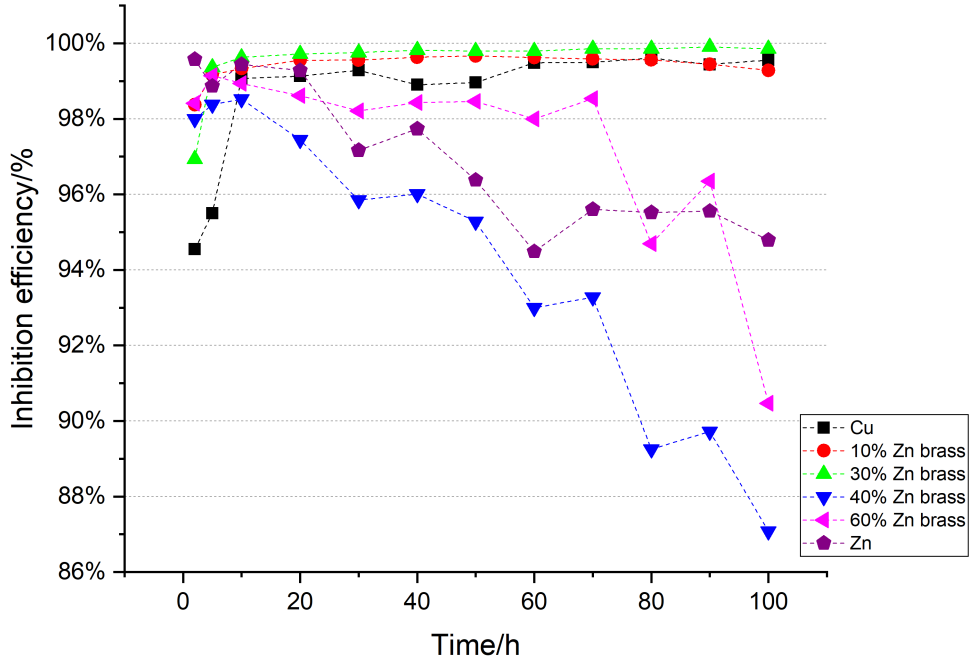

Figure 31: Inhibition efficiencies of group 1 specimens immersed in 100ml 1 mM MBI solution.

In group 2, the inhibition efficiencies for 50% Zn, 70% Zn and 90% Zn brasses are low at the beginning and then increase rapidly. After 20 hours, they all exceed 80% and fluctuate at a small range from that time. For 80% Zn brass, the efficiency fluctuates at around 85%.

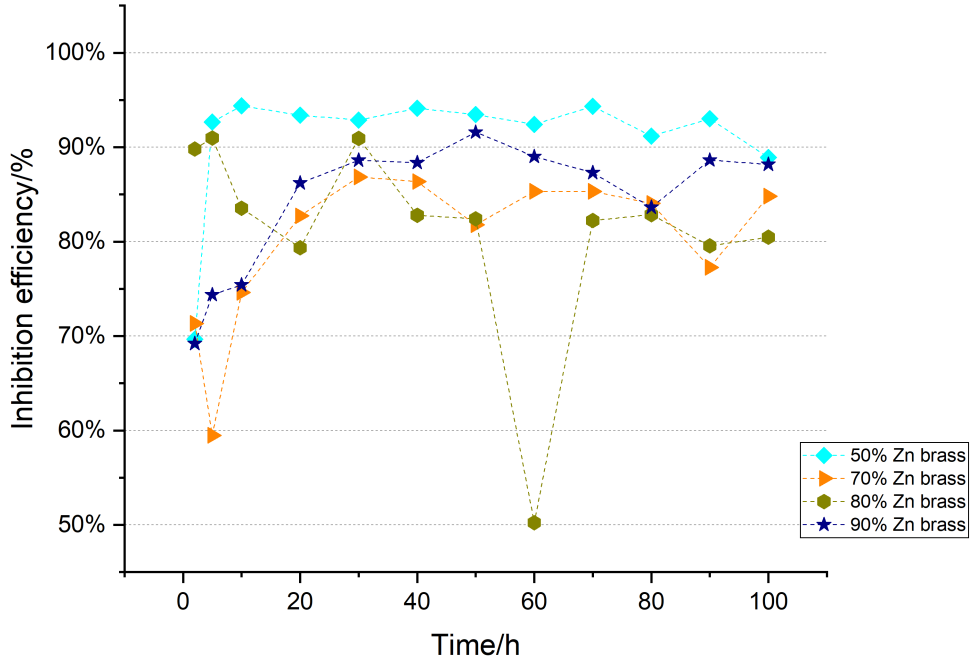

Figure 32: Inhibition efficiencies of group 2 specimens immersed in 100ml 1 mM MBI solution.

Average polarization resistance of each specimen during the whole experimental period is calculated. It is providen in Figur.40. This graph indicates of large polarization resistances at around 1500000 $\Omega \cdot cm^2$ of Cu and alpha brasses which include 10% Zn and 30% Zn brasses. Besides, the polarization resistance of 60% Zn brass is relatively large at about 600000 $\Omega \cdot cm^2$. The remaining specimens all have small polarization resistances which are not more than 200000 $\Omega \cdot cm^2$.

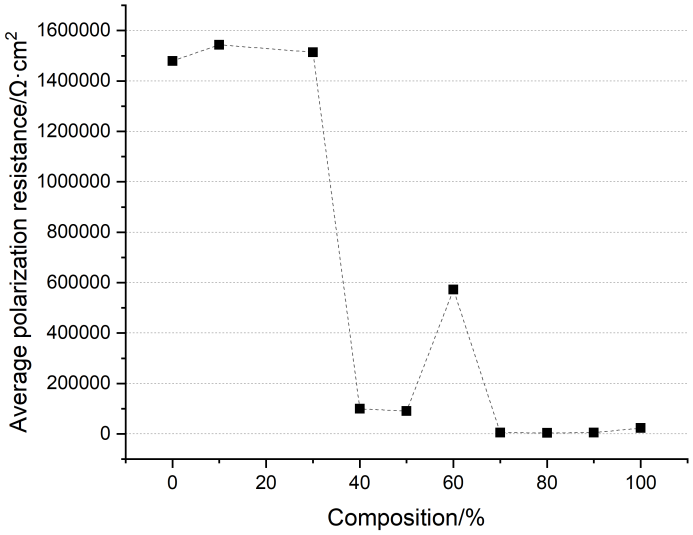

Figure 33: Average polarization resistances of specimens immersed in 100ml 1 mM MBI solution.

3.1.1.2 Specimens in 1 mmol/L 1H-HB-2T solution

Figure 34 illustrates the polarization resistances of specimens in the 1H-HB-2T solution (which also contains 3%wt. NaCl and distilled water). In terms of different types of specimens, pure Cu and alpha brasses which are 10% Zn brass and 30% Zn brass have apparently larger resistances. Besides, the polarization resistance of 60% Zn brass of Gamma phase is relatively high. Polarization resistances of the remaining specimens are too small to be visible on such an axis scale. In the view of the timeline, copper, alpha brasses and 60% Zn brass show a fluctuant ascending tendency. From the graph, it is difficult to judge the trend of other specimens.

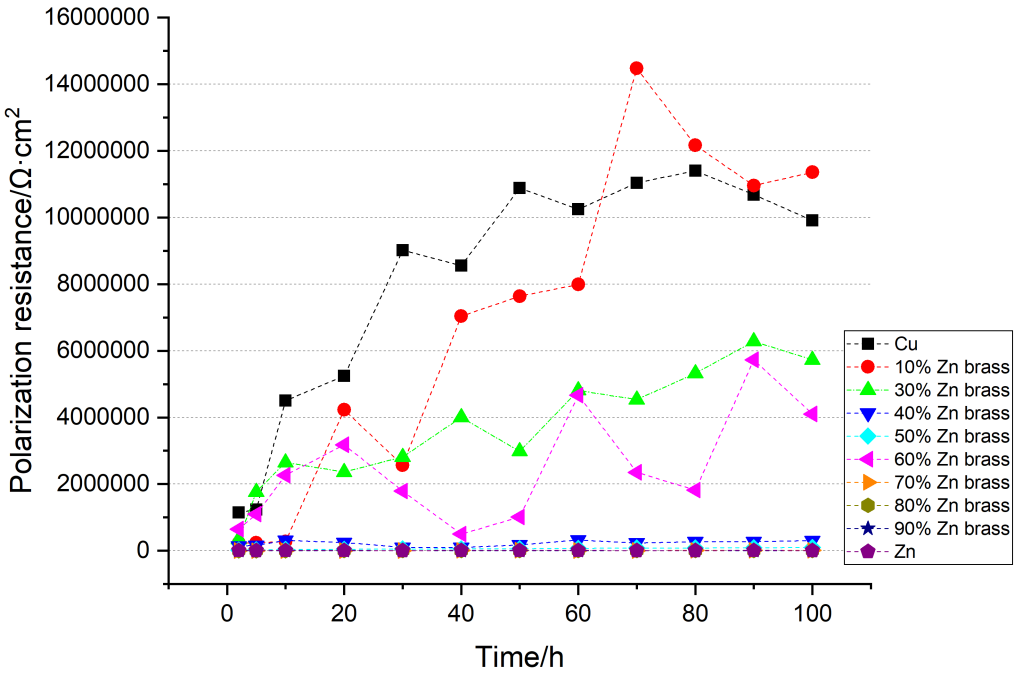

Figure 34: Polarization resistance values of specimens immersed in 100ml 1 mM 1H-HB-2T solution.

Based on Equation.4, inhibition efficiencies of 1H-HB-2T are also divided into 2 groups: group 1 and group 2. group 1 includes copper, 10% Zn brass, 30% Zn brass, 40% Zn brass, 60% Zn brass, zinc while group 2 are 50% Zn brass, 70% Zn brass, 80% Zn brass, 90% Zn brass. The results are shown in Figure 35 and 36. This group division has the same reason as above.

In group 1, 1H-HB-2T for copper, 10% Zn brass, 30% Zn brass maintain high inhibition efficiencies more than 98% while the efficiencies of 40% Zn brass, 60% Zn brass and zinc fluctuate at a high level.

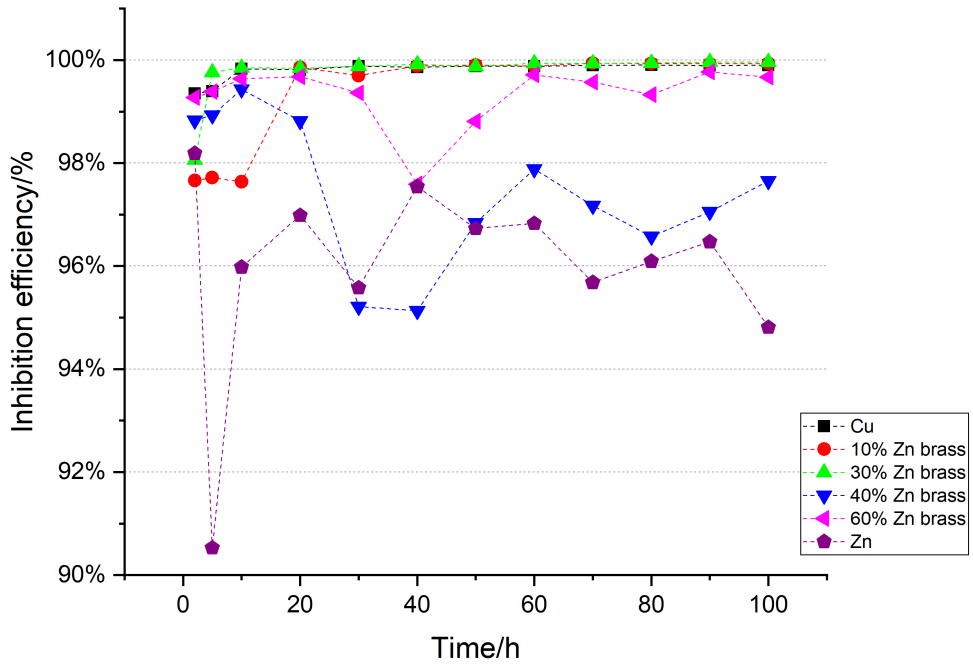

Figure 35: Inhibition efficiencies of group 1 specimens immersed in 100ml 1 mM 1H-HB-2T solution.

In group 2, the inhibition efficiencies for brasses increase with different rates, but they all exceed 85% at the end of the experiment.

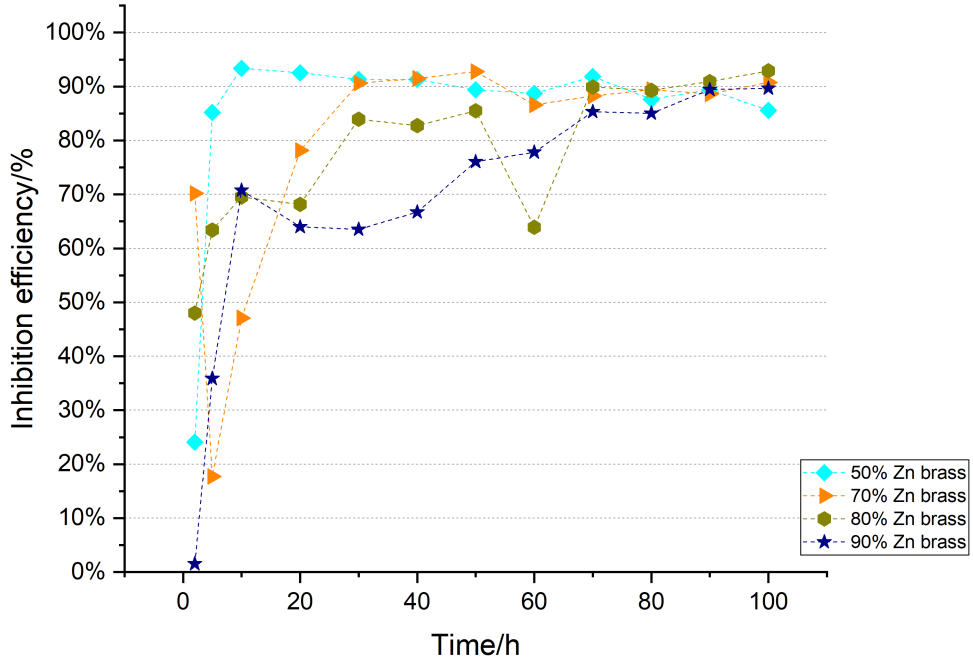

Figure 36: Inhibition efficiencies of group 2 specimens immersed in 100ml 1 mM 1H-HB-2T solution.

The average polarization resistance of each specimen during the whole experimental period is calculated and presented in Figur.37. This graph indicates high polarization resistances of Cu, alpha brasses and a relatively high resistance of 60% Zn brass which are consistent with the conclusions we obtained before.

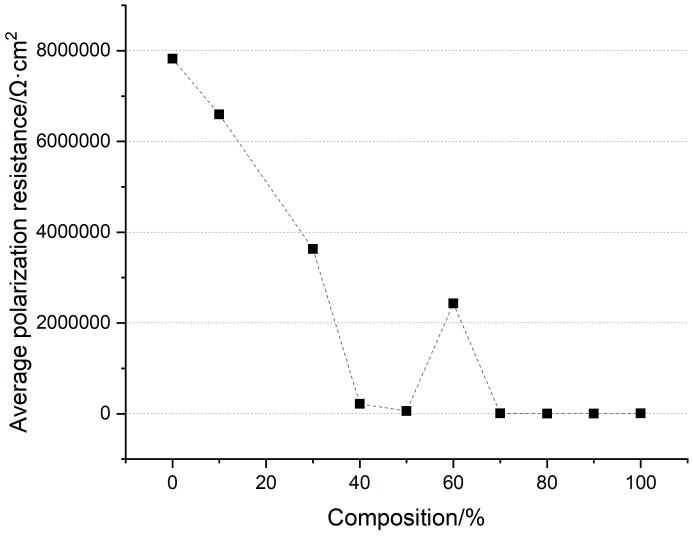

Figure 37: Average polarization resistances of specimens immersed in a 100ml 1 mM MBI solution.

3.1.1.3 Preselection of specimens

This thesis aims to understand the inhibitor mechanisms of inhibitors on Cu, Zn, and different brasses rather than to find the best efficient inhibitor or the most corrosion-resistant brass. So even 60% Zn brass has a relatively high polarization resistance, 50% Zn brass was chosen as a better research objective. There are 2 reasons. The first and the most important reason is that brasses whose Zn contents are more than 50% are too brittle for general use, 50% is the upper limit value for Zn. Secondly, 50% Zn brass is of a single-phase, that is, Beta brass. The study of it helps to understand the function of Beta phase in the corrosion process. Besides 50% Zn brass, Cu and Zn were chosen since they are two basic elements in brasses. So specimens for the next step shrink to Cu, Zn and 50% Zn brass. Replicated LPR measurements have been done and two closest groups of data were used to calculate the average data in the plots. So the accuracy of results was guaranteed.

Figure 40 provides the polarization resistances of Cu in 100ml 1 mM MBI and 1H-HB-2T solutions. The polarization resistance in the 1H-HB-2T solution is higher than that in the MBI solution. And both they show an increase firstly (1H-HB-2T to 70th hour and MBI to 80th hour) and decrease during the rest of the experimental time. This is a typical adsorption–desorption process.

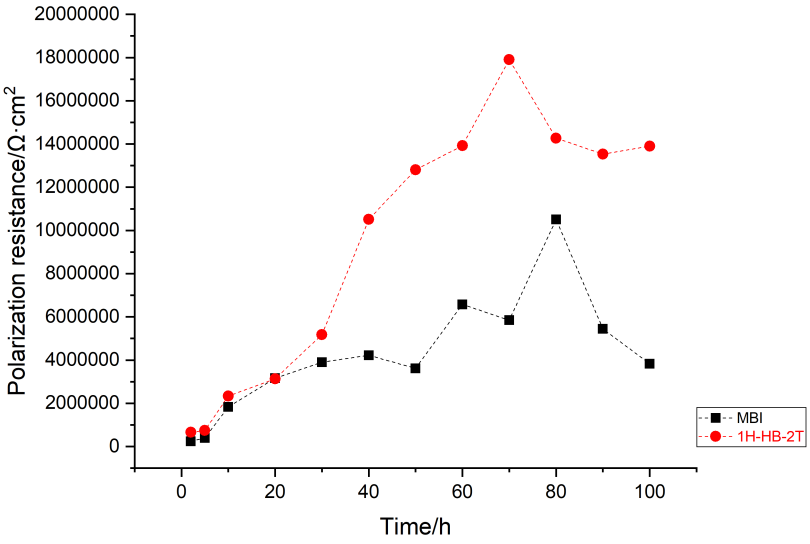

Figure 38: Polarization resistances of Cu immersed in 100ml 1 mM MBI and 1H-HB-2T solutions.

Polarization resistances of 50% Zn brass in 100ml 1 mM MBI and 1H-HB-2T solutions are providen below. The trend of 50% Zn brass is almost the same with that of Cu except that the increase period for 50% Zn brass is longer which is to 90 hours.

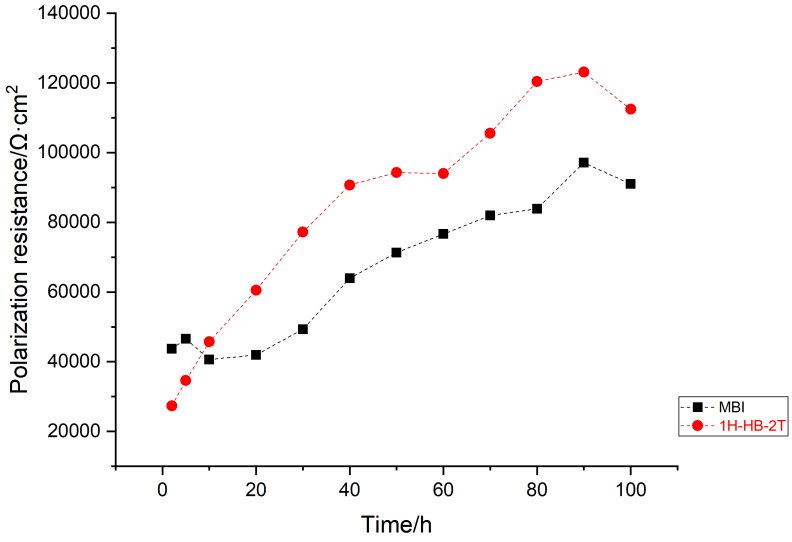

Figure 39: Polarization resistances of 50% Zn brass immersed in 100ml 1 mM MBI and 1H-HB-2T solutions.

Polarization resistances of Zn in 100ml 1 mM MBI and 1H-HB-2T solutions can be seen in Figure 40. Zn shows a completely different trend. Polarization resistance of Zn inthe 1H-

HB-2T solution slightly fluctuates at around 7500 $\Omega \cdot cm^2$. The polarization resistance in the MBI solution sharply drops from 45000 $\Omega \cdot cm^2$ to the same level of that in 1H-HB-2T solution within the beginning 20 hours. Such a decrease at the beginning is likely to be due to the dissolution of the preexisting oxide layer on the surface.

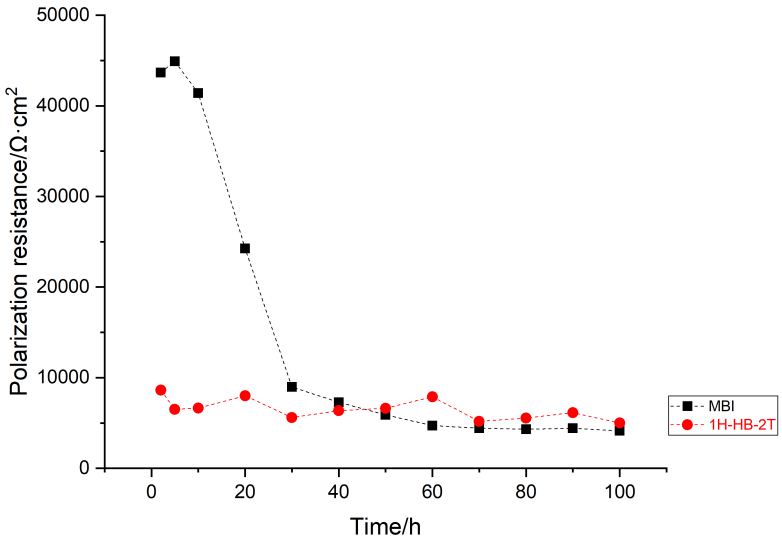

Figure 40: Polarization resistances of Zn immersed in 100ml 1 mM MBI and 1H-HB-2T solutions.

3.1.2 Electrochemical Impedance Spectroscopy (EIS)

The average EIS plots of Cu, Zn and 50% Zn brass are providen below. Each EIS experiment has at least 3 parallel experiments and the two closest groups of data were chosen to calculate the average and eventually the average data points are used to draw the plots.

Various reaction parameters such as charge transfer resistance (R_{ct}), double layer capacitances (C_{dl}) and solution resistance (R_s) could be obtained by EIS results. The impedance plots are not perfect semicircles. This feature could be attributed to frequency dispersion and impedance arcs overlap. The charge transfer values (R_{ct}) are calculated from the difference in impedance at the lower and higher frequencies as suggested by Haruyama et al. [42]. If there is a serious overlap of impedance arcs, it reduces the accuracy of R_{ct} or causes missing data. The double-layer capacitance (C_{dl}) can be calculated by Equation.10, but the frequency at which the imaginary component of the impedance is maximum ($-Z''_{max}$) needs to be exactly found and the involvement of R_{ct} in the equation further reduces the accuracy. So C_{dl} is not discussed in this thesis. R_s corresponds to the impedance at the very high frequency region and it is ignored under normal conditions. So only R_{ct} and the impedance at

the low frequency region which is related to R_p are investigated.

$$C_{dl} = \frac{1}{2f(-Z_{immax})R_{ct}} \tag{10}$$

3.1.2.1 Pure Cu in 1 mmol/L MBI solution

Bode and Nyquist plots of pure Cu in 100ml 1 mM MBI solution for 50 hours are providen in Figure 41 and Figure 42.

In the Nyquist plot, two impedance arcs are exhibited. R_{ct} values are listed in Table.8. The missing data for 2th and 5th hour are associated with the difficulty of identifying the smaller impedance arc. The table shows that R_{ct} increases rapidly and reaches a maximum value after 30 hours. Then it decreases slightly and remains the same. The impedance near the low frequency region generally decreases during the first 30 hours of immersion time followed by a subsequent increase.

In Bode plots, the impedance at the very low frequency which could be roughly regarded as the polarization resistance showed a similar trend with the Nyquist plot. The log|Z| decreases until the 20th hour, it begins to increase after that. From Bode plot (b), two time constants could be observed. The time constant at the low frequency region should be caused by the inhibitor film absorbed on the metallic surface. The other time constant is from the double-layer. The maximum phase angle of the double-layer increases to around 85 degree and its corresponding frequency has a slight shift towards low frequency.

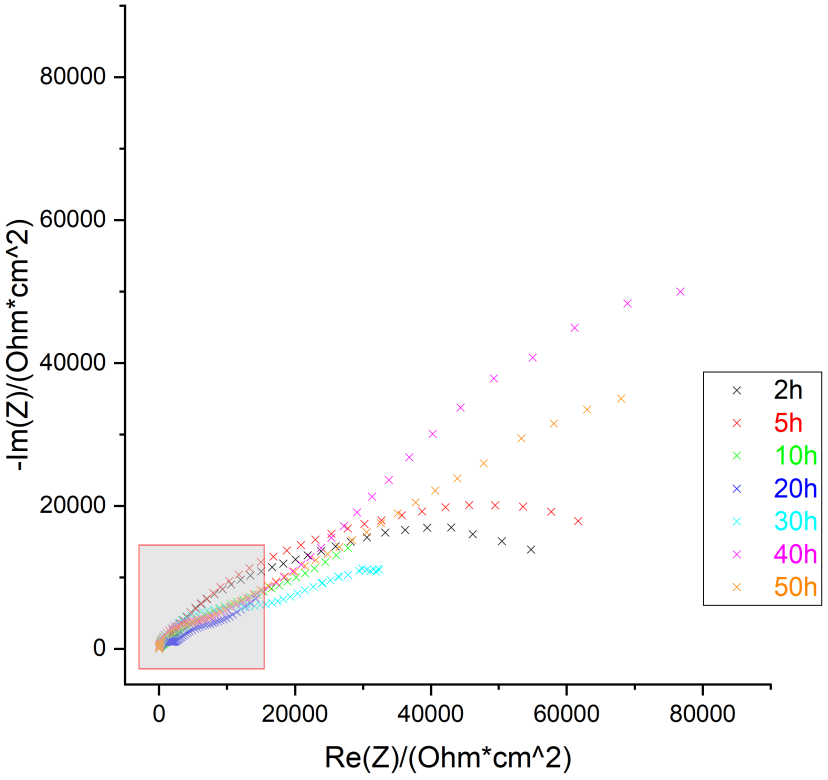

(a) The intact Nyquist plot.

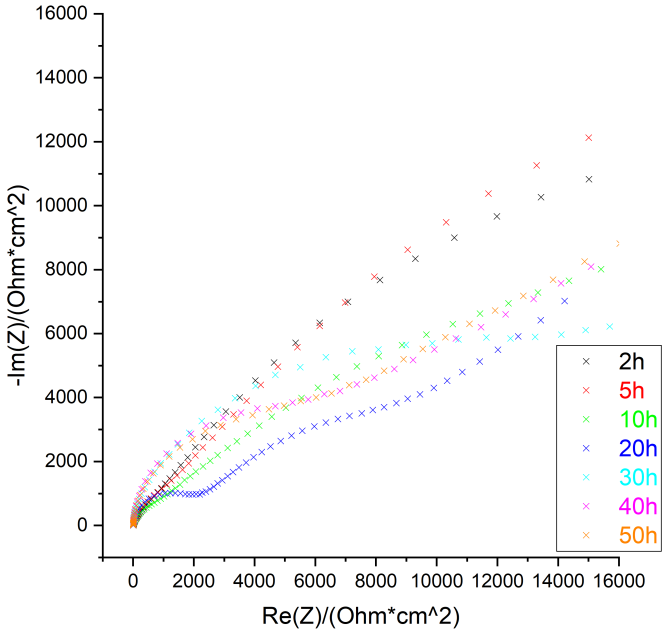

(b) The Nyquist plot at the high frequency region (the square district in the intact plot).

Figure 41: Nyquist plot of pure Cu in 100ml 1 mM MBI solution for 50 hours.

Table 8: R_{ct} obtained from the Nyquist plot.

Time/h	2	5	10	20	30	40	50
R_{ct}/Ohm·cm^2			1250	2500	15000	8000	8000

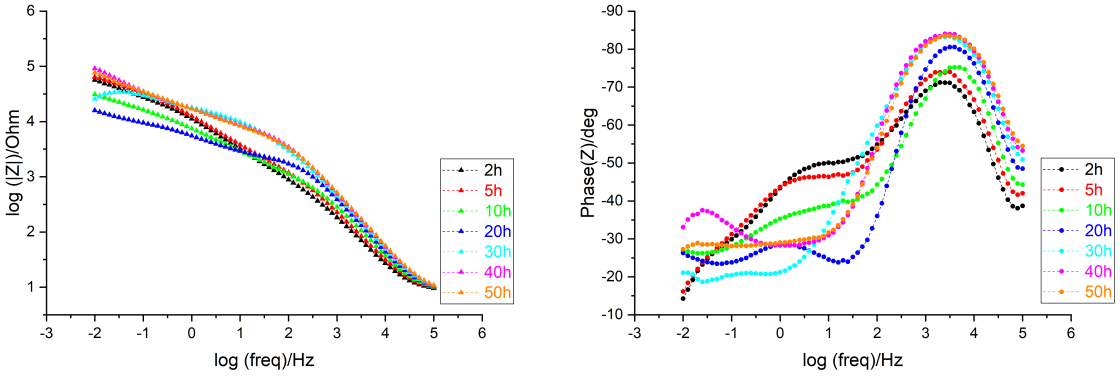

(a) (b)

Figure 42: Bode plots of pure Cu in 100ml 1 mM MBI solution for 50 hours.

3.1.2.2 50% Zn brass in 1 mmol/L MBI solution

Figure 43 and Figure 44 show Bode and Nyquist plots of 50% Zn brass in 100ml 1 mM MBI solution for 50 hours.

In Nyquist plot, at the end period of the experiment, two impedance arcs can be identified. Table.9 shows R_{ct} continues to rise during the whole 50 hours. The impedance at the low frequency region slightly fluctuates all the time.

In Bode plot (a), the impedance at the very low frequency region stays stable and does not have any obvious change with time. In Bode plot (b), there are two time constants at the beginning. The time constant at the high frequency region should be caused by the double layer and the other one at the middle frequency region is likely to come from the corrosion product layer (mainly $Zn(OH)_2$). In the second half of the experiment, a new time constant appears at the low frequency region which could be the inhibitor film. This inhibitor film can be either absorbed on the outer side of the corrosion product layer or the bare metallic surface without corrosion products. The maximum phase angle from the double layer increases gradually because of the decrease of double layer capacity. On the opposite, the maximum phase angle from the corrosion product layer decreases rapidly because the corrosion product layer has increased during the experiment.

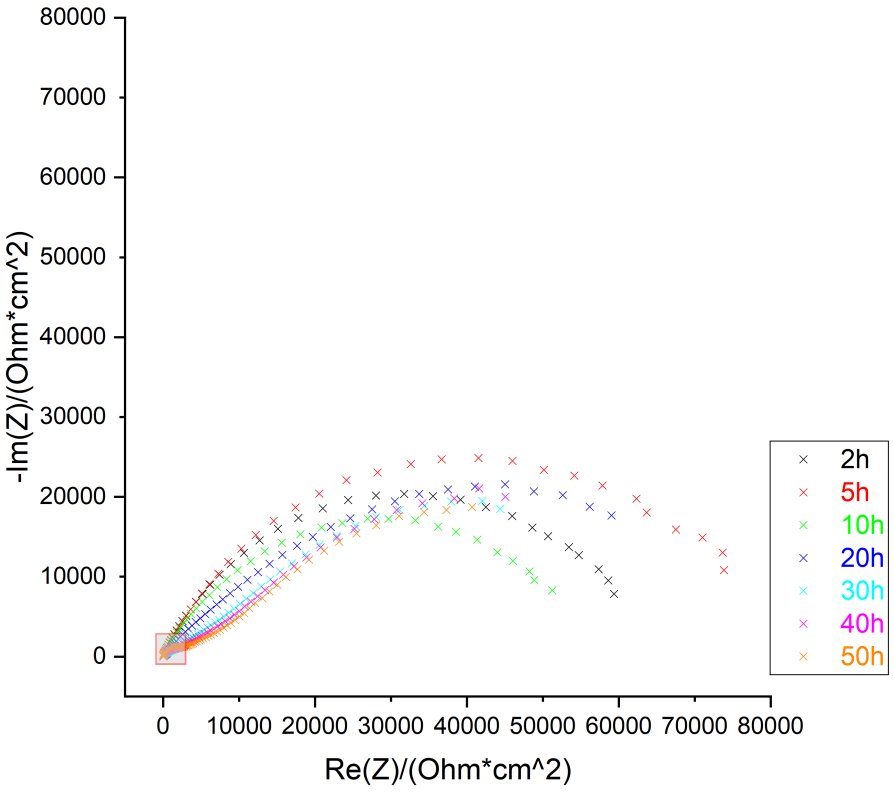

(a) The intact Nyquist plot.

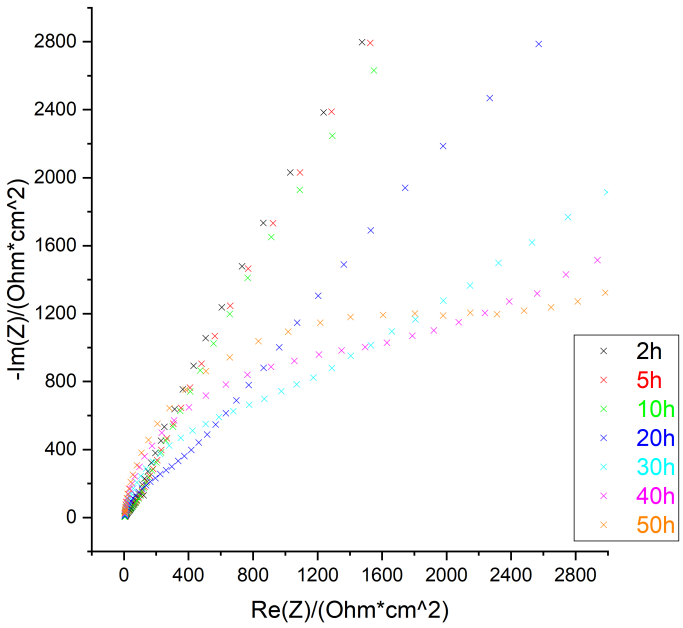

(b) The Nyquist plot at the high frequency region (the square district in the intact plot).

Figure 43: Nyquist plot of 50% Zn brass in 100ml 1 mM MBI solution for 50 hours.

Table 9: R_{ct} obtained from the Nyquist plot.

Time/h	2	5	10	20	30	40	50
R_{ct}/Ohm·cm^2	50	70	70	500	1000	2000	2800

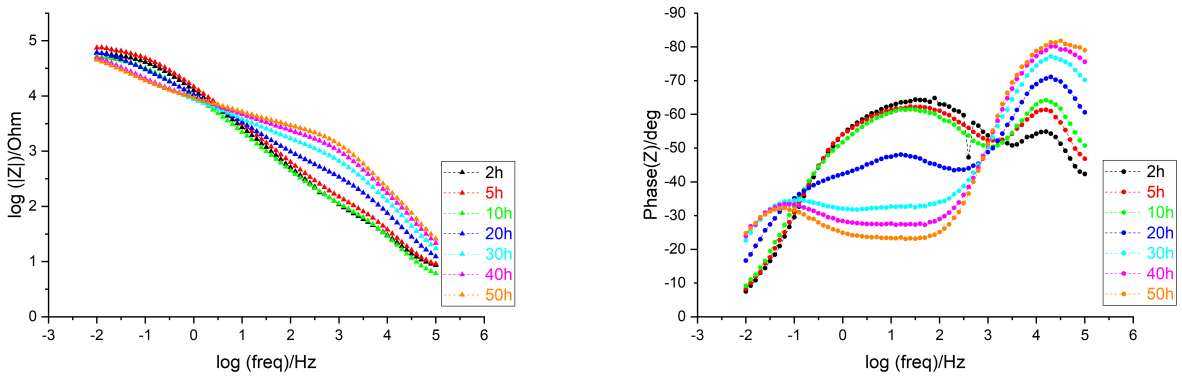

(a) (b)

Figure 44: Bode plots of 50% Zn brass in 100ml 1 mM MBI solution for 50 hours.

3.1.2.3 Pure Zn in 1 mmol/L MBI solution

Figure 45 and Figure 46 provide Bode and Nyquist plots of pure Zn in 100ml 1 mM MBI solution.

There are two oblate, incomplete impedance arcs in the Nyquist plot. Table.10 provides R_{ct} data but a lot of R_{ct} data are missing. The impedance at the low frequency region gradually decreases with the extension of the experiment time.

In Bode plot (a), the log | Z | gradually decreases with the extension of experimental time. In the Bode plot (b), before the 20th hour of the experiment, only one time constant is identified. After that, a new time constant appeared in the low frequency region. The time constant at the low frequency region should be caused by the corrosion products (mainly $Zn(OH)_2$), the other one is due to the double-layer. The maximum phase angle of double layer decreases and its corresponding frequency shifts towards high frequency. Because their values are close, before the 20th hour, they overlap in Bode plot (b). With the process that the area for the double-layer is gradually covered by the corrosion product layer, they can be gradually distinguished.

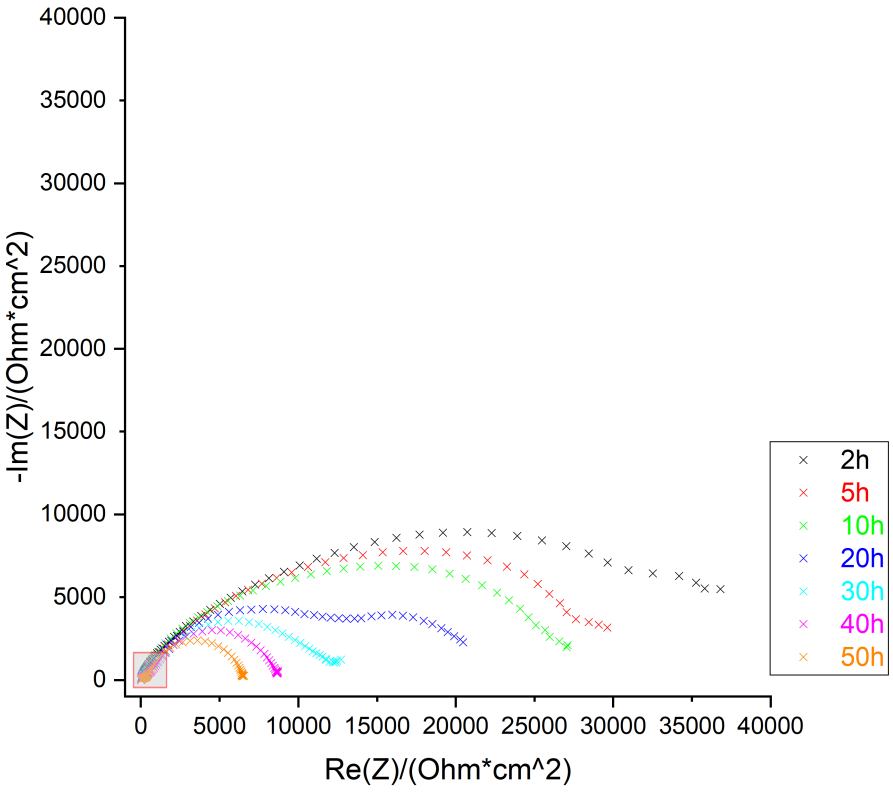

(a) The intact Nyquist plot.

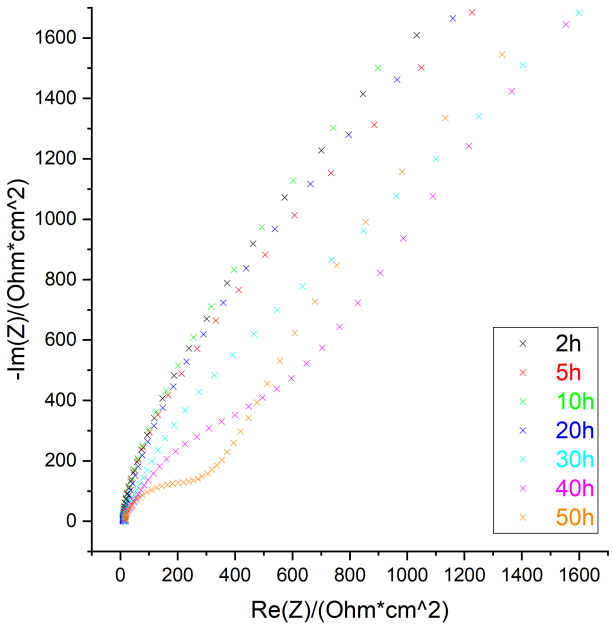

(b) The Nyquist plot at the high frequency region (the square district in the intact plot).

Figure 45: Nyquist plot of pure Zn in 100ml 1 mM MBI solution for 50 hours.

Table 10: R_{ct} obtained from the Nyquist plot.

Time/h	2	5	10	20	30	40	50
R_{ct}/Ohm·cm^2						700	300

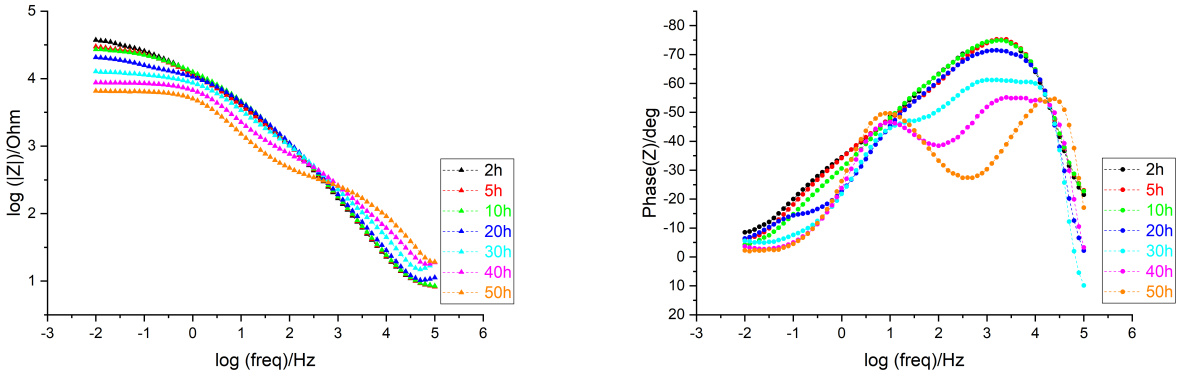

(a) (b)

Figure 46: Bode plots of pure Zn in 100ml 1 mM MBI solution for 50 hours.

3.1.2.4 Pure Cu in 100ml 1 mM 1H-HB-2T solution

Figure 47 and Figure 48 show Bode and Nyquist plots of Cu in 100ml 1 mM 1H-HB-2T solution for 50 hours.

In the Nyquist plot, there are two certifiable impedance arcs. Table.11 shows R_{ct} decreases firstly and then bounces back to the beginning level at the end of the experiment. The impedance at the low frequency region stays the same in the first 10 hours and then decreases along with the increase of time.

In Bode plot (a), log|Z| at the low frequency region begins to slowly decrease after 10-hour exposure. In Bode plot (b), two time constants are observed. From the high frequency region to the low frequency region, the time constants are attributed to the electric double-layer, the MBI inhibitor film sequentially. The maximum phase angle of double-layer increases with the increase of time, while the maximum phase angle of the inhibitor film drops slightly. It has a similarity with that in the MBI solution in essence.

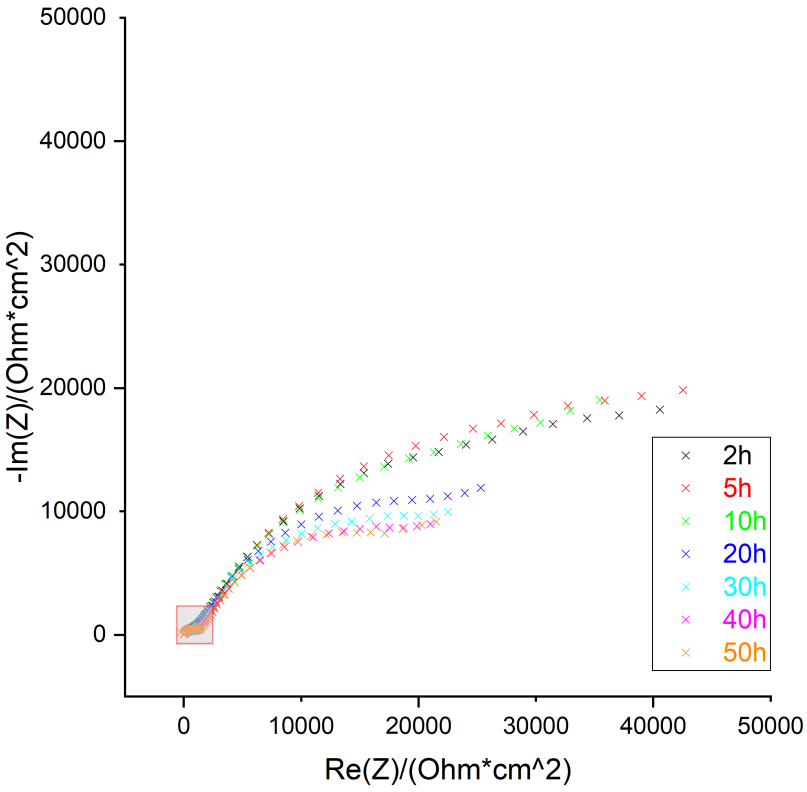

(a) The intact Nyquist plot.

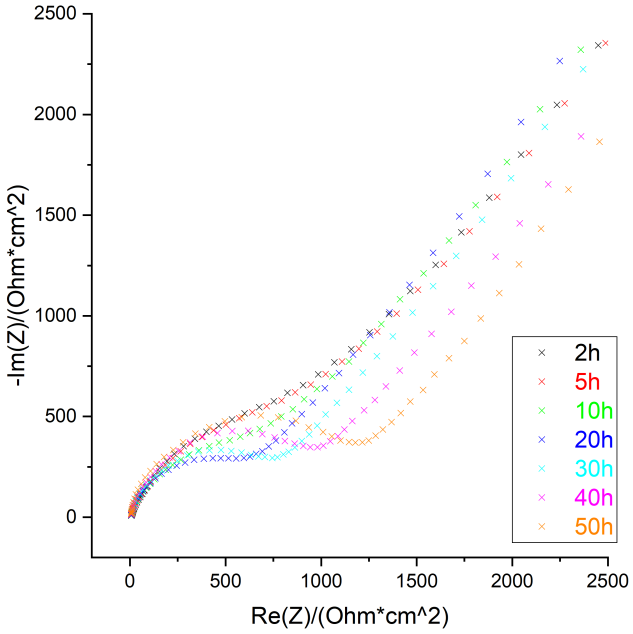

(b) The Nyquist plot at the high frequency region (the square district in the intact plot).

Figure 47: Nyquist plot of pure Cu in 100ml 1 mM 1H-HB-2T solution for 50 hours.

Table 11: R_{ct} obtained from the Nyquist plot.

Time/h	2	5	10	20	30	40	50
R_{ct}/Ohm·cm^2	1250	1250	900	750	900	1100	1250

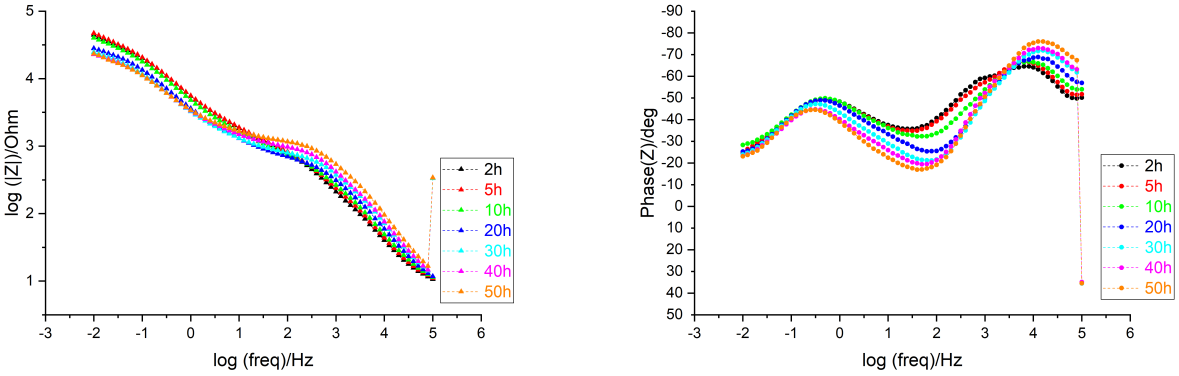

(a) (b)

Figure 48: Bode plots of pure Cu in 100ml 1 mM 1H-HB-2T solution for 50 hours.

3.1.2.5 50% Zn brass in 100ml 1 mM 1H-HB-2T solution

Figure 49 and Figure 50 show Bode and Nyquist plots of 50% Zn brass in 100ml 1 mM 1H-HB-2T solution for 50 hours.

In the Nyquist plot, R_{ct} in Table.12 has a monotonic increase trend. The impedance at the low frequency region rises rapidly at the first 20 hours and then basically remains unchanged.

In Bode plot (a), with the time increase, $\log|Z|$ in the very low frequency region increases a little. Similar to the result of 50% Zn brass in the MBI solution, Bode plot plot (b) graph provides three time constants in total. In the beginning, there is only one clear time constant in the middle region. After 5 hours, another time constant in the high frequency region appears. The last time constant arises in the second half of the experiment. From high frequency to low frequency, time constants are from double-layer, the corrosion product layer and 1H-HB-2T inhibitor film sequentially. This process is complex and a very rough estimation that the double-layer capacity drops, the inhibitor film capacity increases and the corrosion product layer capacity rises with the extension of time.

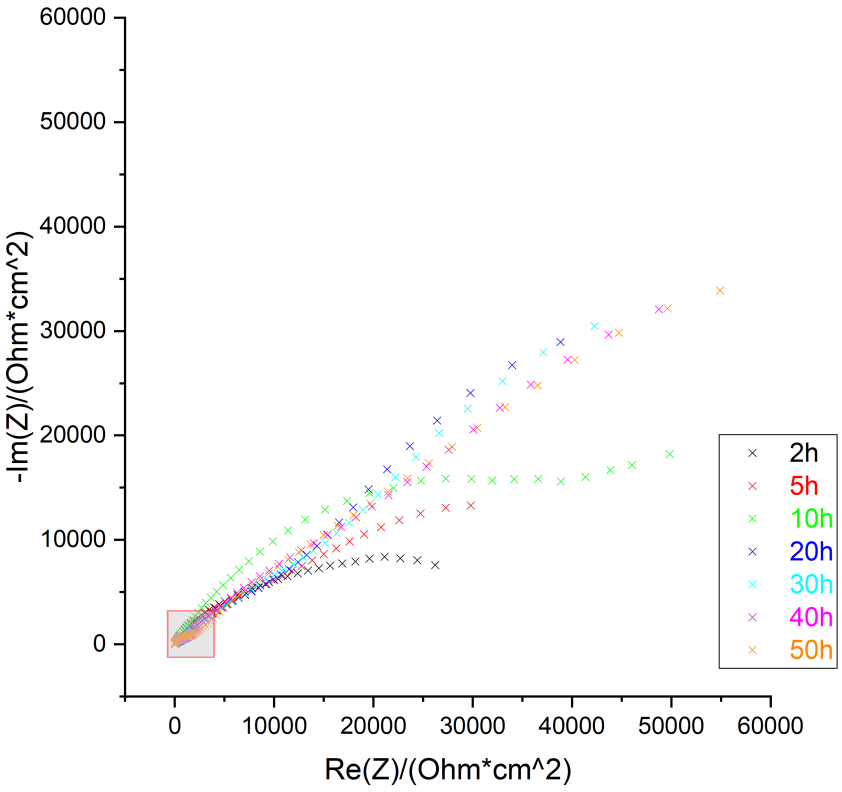

(a) The intact Nyquist plot.

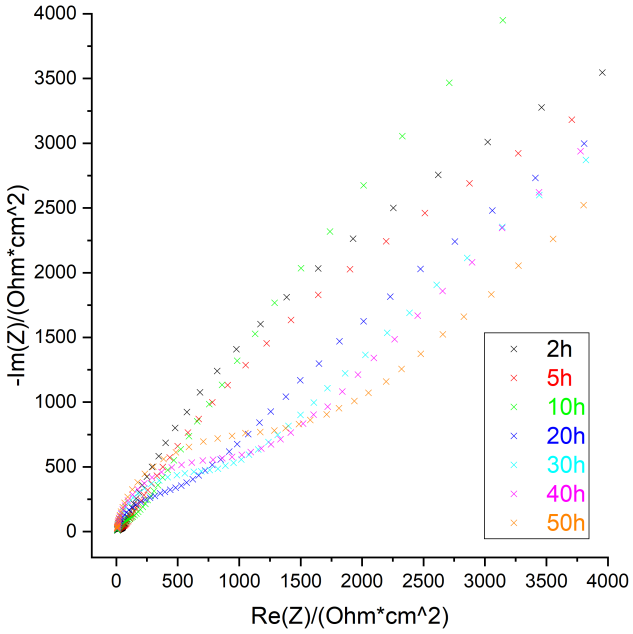

(b) The Nyquist plot at the high frequency region (the square district in the intact plot).

Figure 49: Nyquist plot of 50% Zn brass in 100ml 1 mM 1H-HB-2T solution for 50 hours.

Table 12: R_{ct} obtained from the Nyquist plot.

Time/h	2	5	10	20	30	40	50
R_{ct}/Ohm·cm^2	50	70	100	700	1000	1200	1500

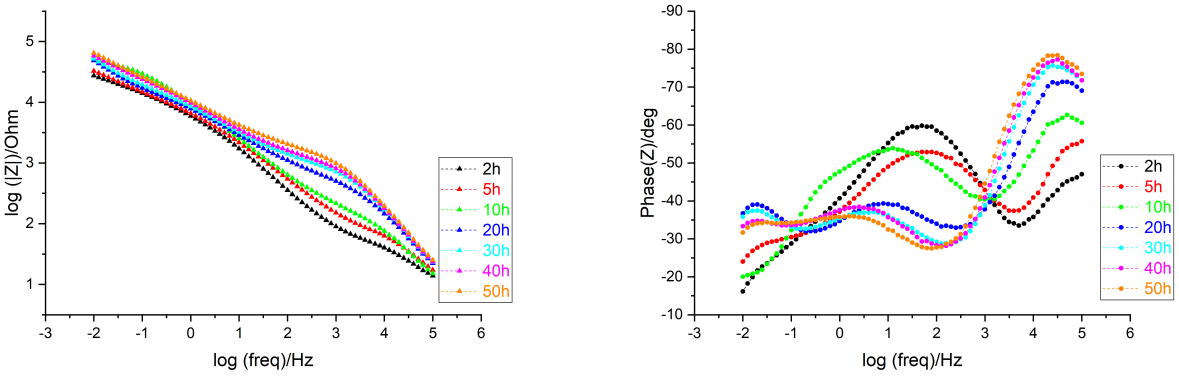

(a) (b)

Figure 50: Bode plots of 50% Zn brass in 100ml 1 mM 1H-HB-2T solution for 50 hours.

3.1.2.6 Pure Zn in 100ml 1 mM 1H-HB-2T solution

Figure 51 and Figure 52 provide Bode and Nyquist plots of pure Zn in 100ml 1 mM 1H-HB-2T solution.

In the Nyquist plot, there is only one oblate impedance arc within the first 5 hours and after that, the second arc appears in the low frequency region. Table.13 provides R_{ct} of the second period of the experiment. R_{ct} increases from the 20th hour to the 40th hour and then keeps stable. The impedance at the low frequency region fluctuates at around 6000 $\Omega\Delta cm^2$.

In Bode plot (a), the log|Z| in the low frequency region keeps steady. In the Bode plot (b), before the 5th hour of the experiment, only one time constant is identified. After that, a new time constant appears in the high frequency region. The time constant in the low frequency region should be mainly caused by the corrosion product layer, the other one is due to the double-layer. According to the information above, the double-layer capacity drops, the corrosion product capacity increases in the process.

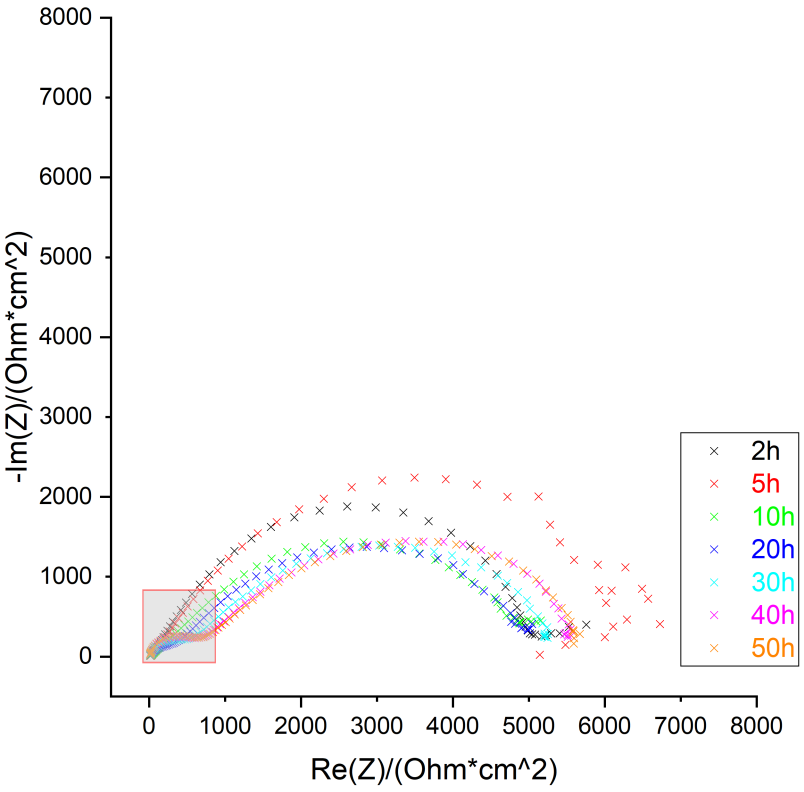

(a) The intact Nyquist plot.

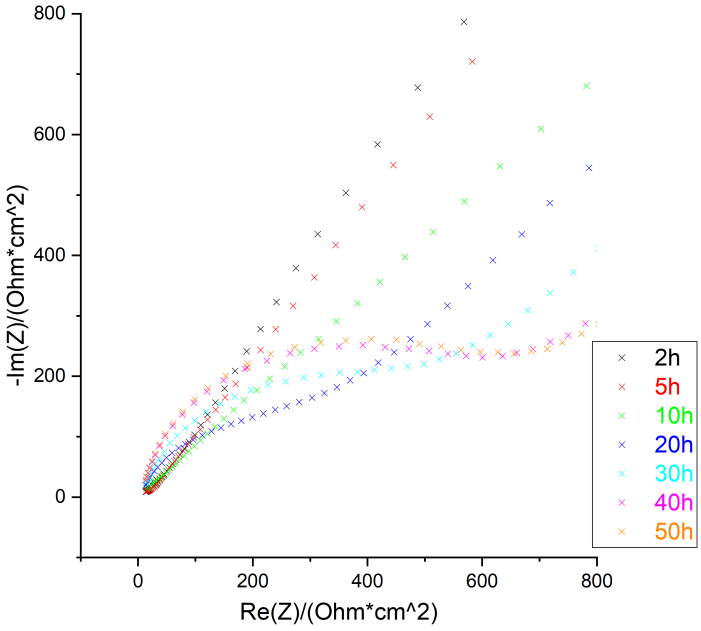

(b) The Nyquist plot at the high frequency region (the square district in the intact plot).

Figure 51: Nyquist plot of pure Zn in 100ml 1 mM 1H-HB-2T solution for 50 hours.

Table 13: R_{ct} obtained from the Nyquist plot.

Time/h	2	5	10	20	30	40	50
R_{ct}/Ohm·cm^2				300	550	700	700

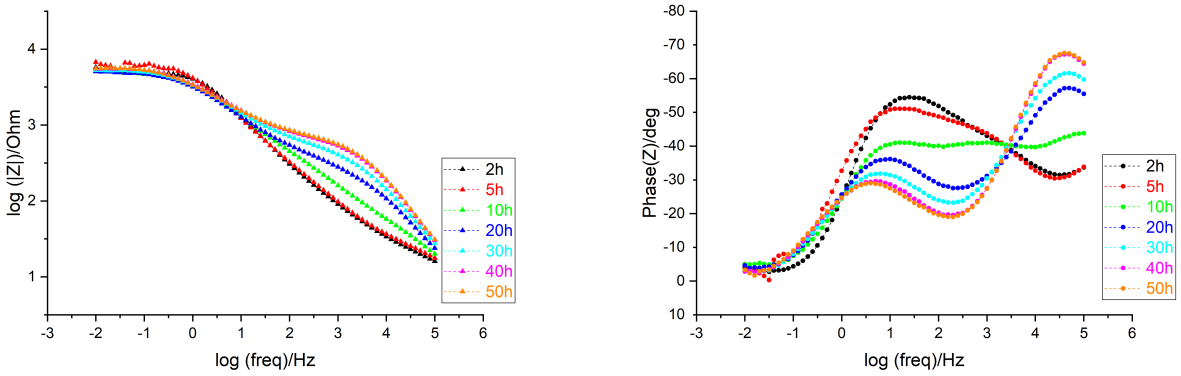

(a) (b)

Figure 52: Bode plots of pure Zn in 100ml 1 mM 1H-HB-2T solution for 50 hours.

3.1.3 Summary of electrochemical measurements

As for different brasses, alpha brasses (10% Zn brass and 30% Zn brass) have the highest corrosion resistance among the studied materials.. And generally, with an increased zinc content, the corrosion resistance of brass decreases except for the gamma brass specimen which contains 60% Zn. In terms of the two inhibitors, 1H-HB-2T has a higher inhibition ability than MBI. According to the EIS results, plural time constants exist in EIS plots which indicates both the inhibitor film and the corrosion product layer affect the corrosion process.

3.2 Fourier Transform Infrared Spectroscopy(FTIR)

Miloev et.al., [23, 41] mentioned multiple adsorption modes of MBI molecules on the Cu surface defined by density functional theory (DFT) calculations as shown schematically in Figure 53. Other adsorption modes are also introduced in the work of Ingrid Miloev, Nataa Kovaevi, and Anton Kokalj. But the common point of all adsorption modes is that only either or both N and S atoms play a role in the formation of chemical bonds. This will affect the FTIR spectrum of corresponding functional groups. As for 1H-HB-2T, it is very likely to have the same adsorption mode with MBI since they have similar structures.

(a) (b)

Figure 53: Optimized structures of MBI molecules adsorbed on Cu(1 1 1) (left panels) and the [MBI–Cu_{ad}] monomer complex (right panels). Color coding of atoms is also indicated: H is cyan, C is yellow, N is sky-blue, and Cu is colored copper-brown with color becoming darker as going from surface toward the bulk. Bond lengths are specified in Åunits. [41]

In this section, inhibitors (MBI and 1H-HB-2T) were dissolved in the THF solution to prepare 100ml 1 mM solution. Then, ex-situ and in-situ FTIR spectrum of Cu and Zn in MBI and 1H-HB-2T THF solutions were collected. Before analysis, FTIR spectroscopy was base-line corrected and smoothed initially for distinguishing peaks of each functional group easily. The infrared absorption frequencies used in the analysis of the FTIR spectrum are listed in Table.14 [43, 44]. Although the chemical environments of functional groups in this chart do not completely match that of the experiment, this table still could be used as the reference for identifying functional groups.

Table 14: Infrared absorption frequencies of functional groups.

Functional group name	Chemical environment	Type of vibration	Frequency (cm^{-1})	Intensity
C-H	-CH_3	δ	1450 and 1375	m
	Aromatics	ν	3150-3050	s
		γ	900-690	s
C=C	Aromatic		1600 and 1475	m-w
N-H	Primary and secondary amines and amides	ν	3500-3100	m
		δ	1640-1550	m-s
C-N	Amines		1350-1000	m-s
C=N	Imines and oximes		1690-1640	m-s
S-H	Mercaptans		2550	w

The meanings of some common symbols used are providen:

ν stretch vibration

δ bend vibration

γ out-of-plane bend vibration

s strong

m medium

w weak

subst. the substituted function groups of benzene ring

3.2.1 Ex-situ Fourier Transform Infrared Spectroscopy(FTIR)

The ex-situ FTIR spectrums of Cu and Zn are shown in Figure 54 and Figure 54. Due to the fringe interference and the overlap of peaks, only part of peaks that are clear and meaningful are concentrated.

3.2.1.1 The ex-situ FTIR spectrum in 1 mM MBI THF solution

For 50% Zn brass and pure Zn, N-H and C-H bonds can be easily identified since their stretch vibration peaks are apparent at about 3400 cm^{-1} and 2900 cm^{-1} respectively. Other functional groups such as C=N, C=C, and N-H can be pointed at the range of about 1700-1400 cm^{-1}. Also, the stretch vibration peak of C-N at around 1350 cm^{-1}, the bend vibration peak of C-H at the range of 1200-1050 cm^{-1} and the out-of-plane bend vibration of C-H at around 900 cm^{-1} are observed. For pure Cu, the intensities of some peaks deceased and the peak of stretch vibration of the N-H bond disappeared totally. Other information is almost the same.

As the analysis above, the frequency peaks of vibrations of most function groups are observed in ex-situ FTIR. However, there is no evidence of the existence of S-H bonds, because, for mercapto molecules, thione tautomers are by about 0.5 eV more stable than thiols (as standalone) and thiols could dissociate barrier-less or almost so (S–H bond cleavage) [23]. Another noteworthy phenomenon is that there is no N-H peak for Cu surface while it appears for both 50% Zn brass and Zn surfaces. One possible explanation is that N-H attends the bond formation of inhibitor molecules and the copper surface. However, this needs more evidence to support it. Besides, near 659 cm^{-1}, there might be an absorption of

the C-S bond, but it does not appear. This can be caused either by the limited optimal spectra collection range of the FTIR machine or by the weakness of the vibration of this bond.

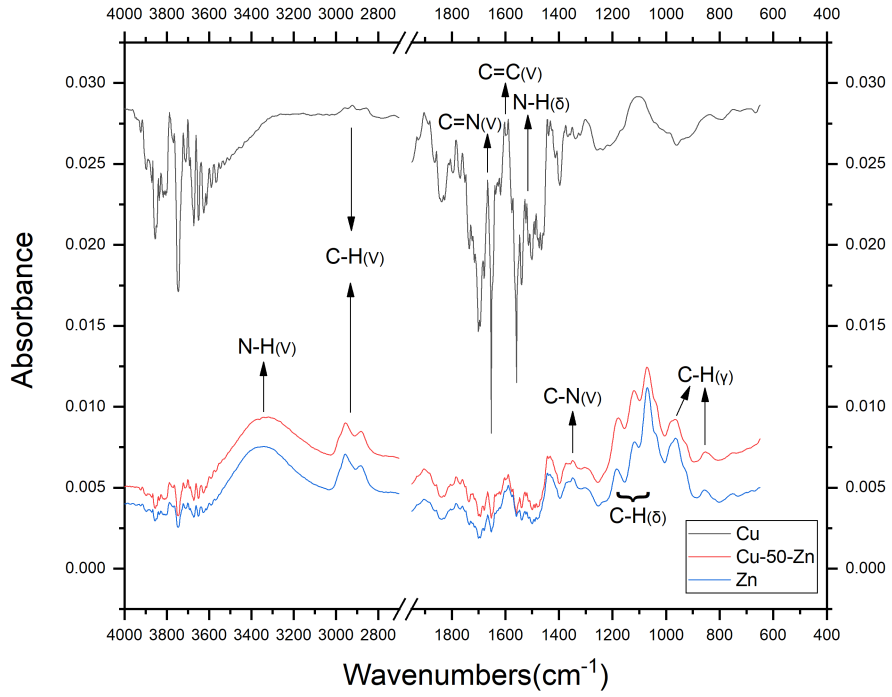

Figure 54: Ex-situ FTIR spectra of 1 mmol/100ml MBI solution.

3.2.1.2 The ex-situ FTIR spectrum in 1 mM 1H-HB-2T THF solution

In these experiments, the fringe effect is serious which leads to the absence of the information at the range of 2300 to 1500 cm^{-1}. For all the three kinds of samples, they have analogous absorption spectrum. The stretch vibration peaks of N-H, C-H, C=C, and C-N bonds are located at 3400 cm^{-1}, 2900 cm^{-1}, 1470 cm^{-1} and 1300 cm^{-1} respectively. Besides, near 1000 cm^{-1}, there are two absorption peaks. The peak which is a bit more than 1000 cm^{-1} probably was C-N peak. The peaks of frequency lower than 1000 cm^{-1} represent the bend and out-of-plane bend vibration of C-H.

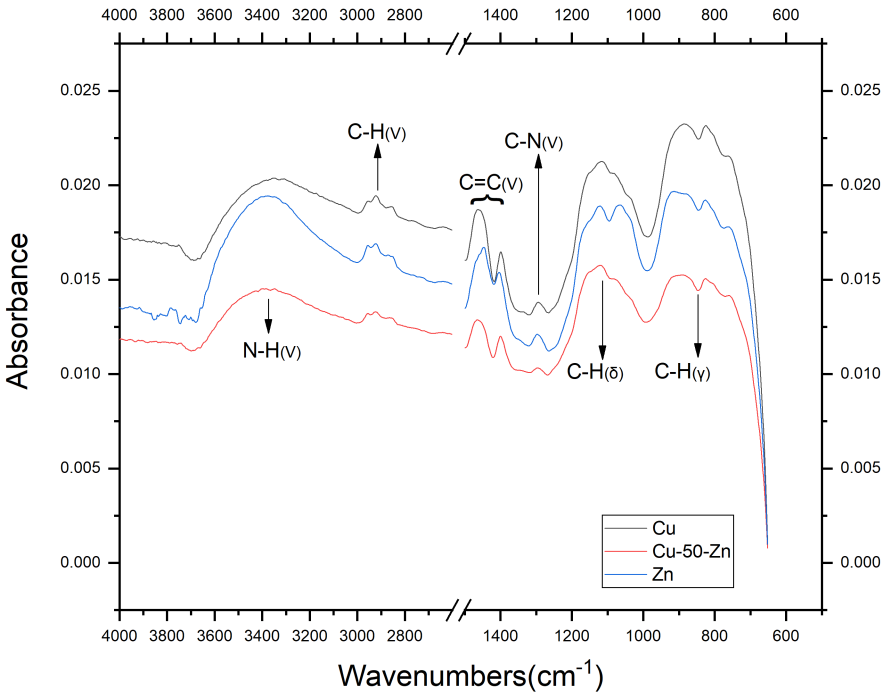

Figure 55: Ex-situ FTIR spectra of 1 mmol/100ml 1H-HB-2T THF solution.

One question here is a peak at around 3400 cm^{-1} appears. This frequency could be the characteristic frequency of N-H, but according to the 1H-HB-2T structure in Figure 9, it does not have the N-H bond. The most reasonable explanation is that 1H-HB-2T spontaneously transforms from thiol to thione just as Figure 11 shows.

3.2.2 In-situ Fourier Transform Infrared Spectroscopy(FTIR)

3.2.2.1 The in-situ FTIR spectrum of Pure Cu in 1 mM MBI THF solution

The base-line corrected and smoothed in-situ FTIR spectrum of a thin copper film deposited on the Ge crystal in 1 mM MBI THF solution is shown in Figure 56. Peaks corresponding to these functional groups are signed in this figure and their relative peak intensity change within 10 hours is calculated and shown in Figure 57.

In Figure 56, some peaks including the stretch, bend, and out-of-plane bend vibration peaks of C-H at 2983 cm^{-1}, 1083 cm^{-1} and 987 cm^{-1} are inverted downward. This phenomenon is likely to be caused by the specific effective optical path length. Some optical effects such as the electric field standing wave effect can influence peak shapes [45]. These peaks could

be avoided by changing other ATR crystal such as ZnSe or diamond. Since the inversion of peaks does not affect the next analysis, they are accepted with a decreased reliability. Besides the inverted peaks of C-H, most peaks are inverted at the beginning. This should be caused by the unstable state on the surface. For example, the absorption of H_2O and CO_2 from the air at the beginning can cause interference on optical path length. Other information from the graph is normal. C=N stretching vibration causes a peak at the wavenumber around 1672 cm^{-1}, compared with the peaks that appear at 1591 cm^{-1} produced by C=C stretching vibration and 1529 cm^{-1} produced by N-H stretching vibration.

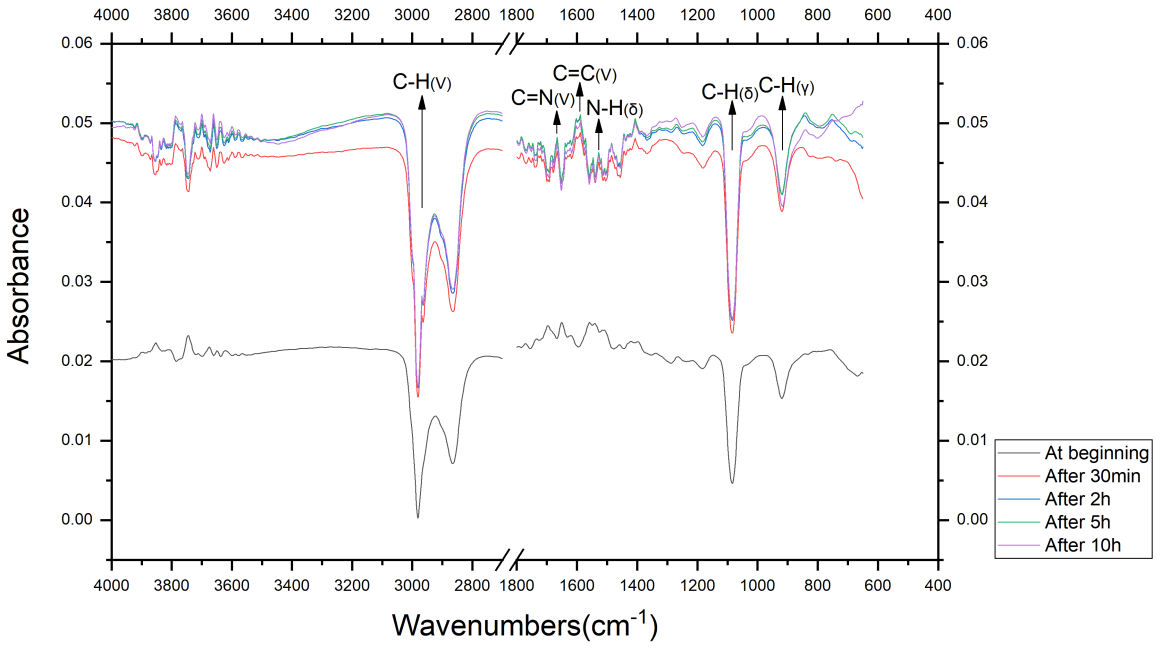

Figure 56: In-situ FTIR spectra of Cu in 100ml 1 mM MBI solution.

Because some peaks (vibration peaks of C-H) are inverted, their absolute peak intensities are used in Figure 57 and other intensities are normally shown. From the graph, the relative peak intensities show a similar trend. They rise rapidly within the first 2 two hours and then increase very slowly until the 10th hour. It means that the adsorption of each MBI functional group on the Cu surface increases rapidly and almost finishes within the first 2 two hours. Afterward, they remain stable with a small increase. This process suits some facts that the adsorption process is rapid and once the equilibrium of adsorption and desorption achieved, it would not have a substantial increase anymore. Besides, another conclusion that could be obtained is the functional groups shown in the figure do not attend the bond formation between the inhibitor molecules and the copper film. After 10 hours, due to the serious dissolution of thin film, the results are unbelievable and are not providen here.

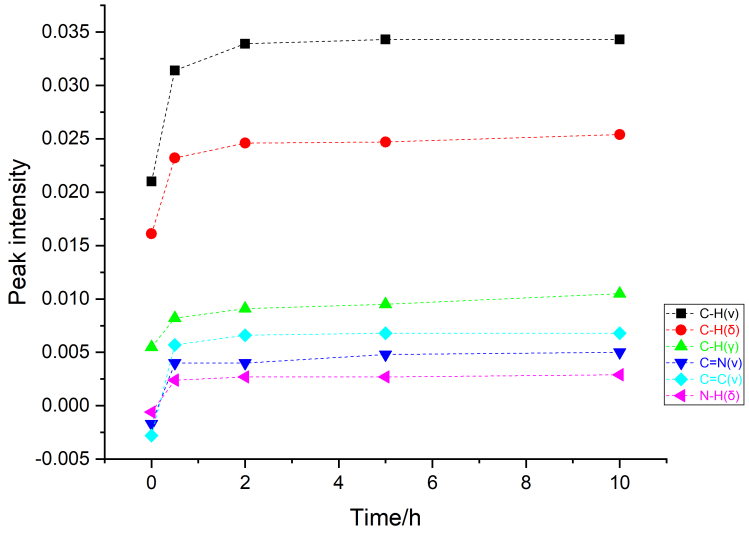

Figure 57: Peak intensity values of Cu from MBI FTIR spectra.

3.2.2.2 The in-situ FTIR spectrum of Pure Cu in 1 mM 1H-HB-2T THF solution

The base-line corrected and smoothed in-situ FTIR spectrum of a thin copper film deposited on the Ge crystal in 1 mM 1H-HB-2T THF solution is shown in Figure 58. Peaks corresponding to these functional groups are signed in this figure and their relative peak intensity change within 10 hours is calculated and shown in Figure 59.

Figure 58 provides similar information with Figure 56. There are peaks including the stretch, bend and out-of-plane bend vibration of C-H at 2989 cm^{-1}, 1103 cm^{-1} and 929 cm^{-1}. Besides, C=C stretch vibration causes a peak at the wavenumber around 1589 cm^{-1}, compared with the peaks that appear at 1531 cm^{-1} produced by N-H bend vibration and 1272 cm^{-1} produced by C-N stretch vibration. The peak at around 2360 cm^{-1} caused by CO_2 is noise. In the beginning, some inverted peaks such as C=C stretch peaks are observed due to the unsteady state on the surface.

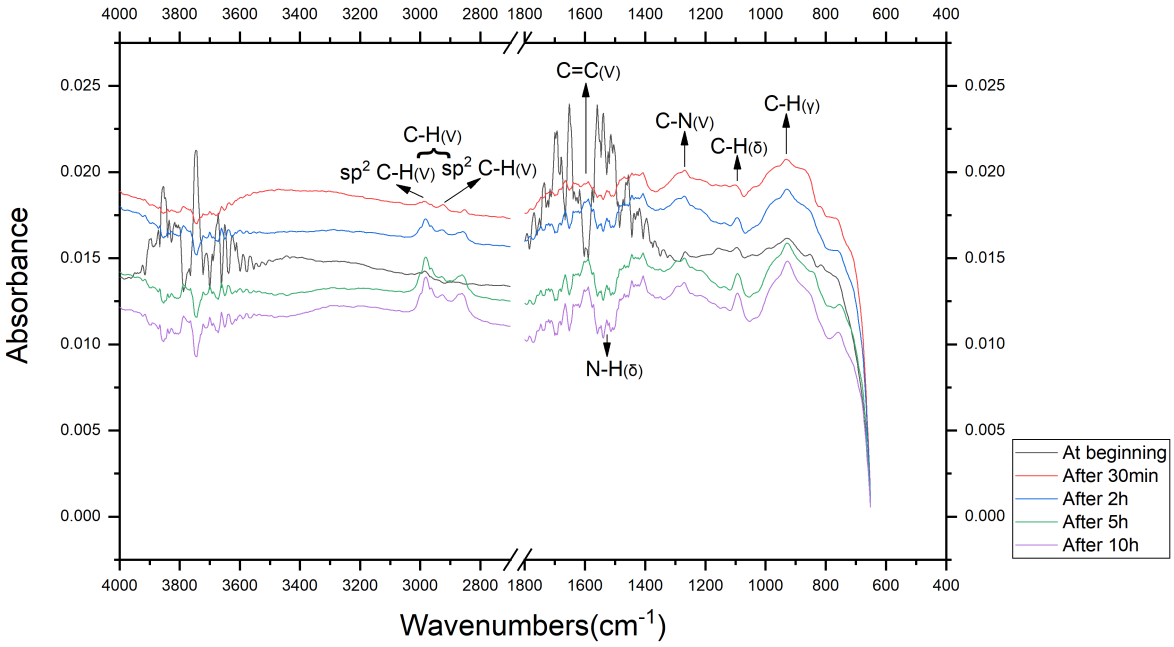

Figure 58: In-situ FTIR spectra of Cu in 100ml 1 mM 1H-HB-2T solution.

As shown in Figure 59, most peaks show two periods in intensity, that is, the rapid increase period and the slow increase period. The intensities for most functional groups rise rapidly for the first half an hour and then keep the slow increase until the 10th hour. This process of 1H-HB-2T is the same as that of MBI on the copper surface. However, it seems that the adsorption of 1H-HB-2T is faster than that of MBI and almost finishes within half an hour on the Cu surface.

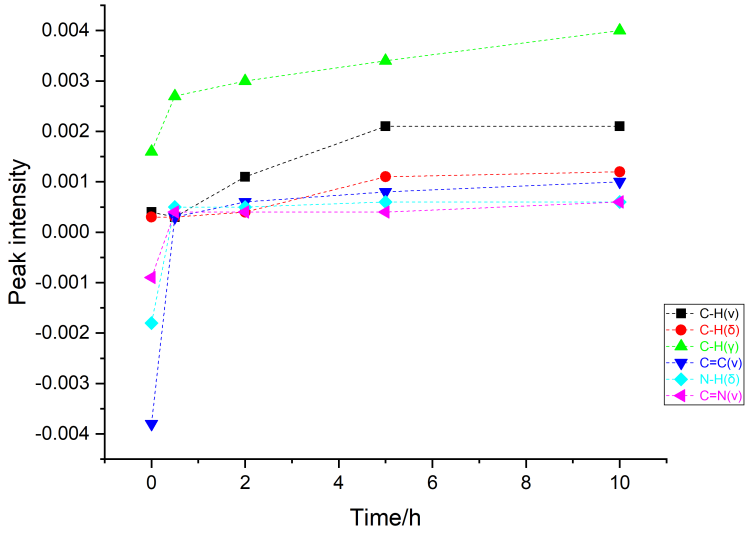

Figure 59: Peak intensity values of Cu from 1H-HB-2T FTIR spectra.

3.2.2.3 The in-situ FTIR spectrum of Pure Zn in 1 mM MBI THF solution

The base-line corrected and smoothed in-situ FTIR spectrum of thin zinc film deposited on the Ge crystal in 1 mM MBI THF solution is shown in Figure 60. Peaks corresponding to these functional groups are signed in this figure and their relative peak intensity change within 10 hours is calculated and shown in Figure 61.

The stretch, bend and out-of-plane bend vibration of C-H are located at 2989 cm^{-1}, 1083 cm^{-1} and 748 cm^{-1} respectively. C=N stretching vibration causes a peak at the wave number around 1666 cm^{-1}, compared with the peaks that appear at 1589 cm^{-1} produced by C=C stretching vibration and 1527 cm^{-1} produced by N-H stretching vibration. The peak at around 2360 cm^{-1} caused by CO_2 is noise. In the beginning, some inverted peaks such as C-H stretch peaks are observed due to the unsteady state on the surface.

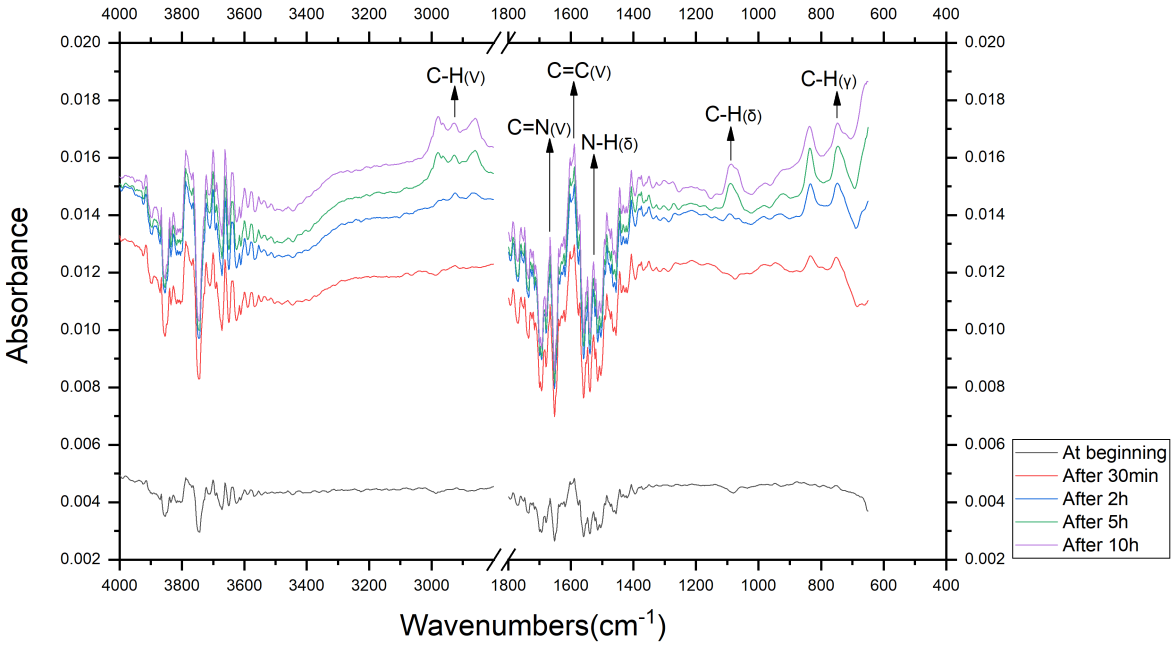

Figure 60: In-situ FTIR spectra of Zn in 100ml 1 mM MBI solution.

Two time periods can also be roughly divided. Within the first 5 hours, the intensities of functional groups have different but relatively high increase rates. After that, they keep the slow increase until the 10th hour. The adsorption process finishes in 5 hours and then surface equilibrium has achieved.

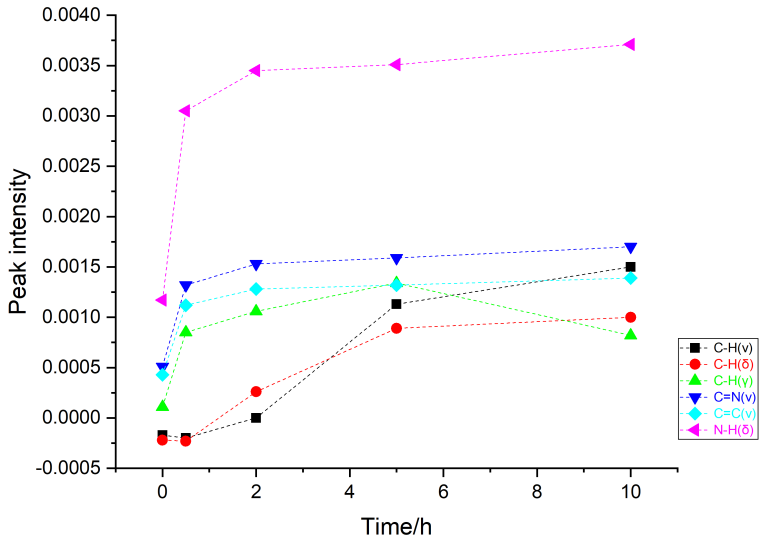

Figure 61: Peak intensity values of Zn from MBI FTIR spectra.

3.2.2.4 The in-situ FTIR spectrum of Pure Zn in 1 mM 1H-HB-2T THF solution

The base-line corrected and smoothed in-situ FTIR spectrum of thin zinc film deposited on the Ge crystal in 1 mM MBI THF solution is shown in Figure 62. Peaks corresponding to these functional groups are signed in this figure and their relative peak intensity change within 10 hours is calculated and shown in Figure 63.

The stretch, bend and out-of-plane bend vibration of C-H are found at 2981 cm^{-1}, 1103 cm^{-1} and 916 cm^{-1} respectively. C=N stretching vibration causes a peak at the wave number around 1666 cm^{-1}, compared with the peaks that appear at 1590 cm^{-1} produced by C=C stretching vibration and 1527 cm-1 produced by N-H stretching vibration. The peak at around 2360 cm^{-1} caused by CO_2 is noise. This experiment seems to have good stability from beginning. No inverted peak is observed in the graph.

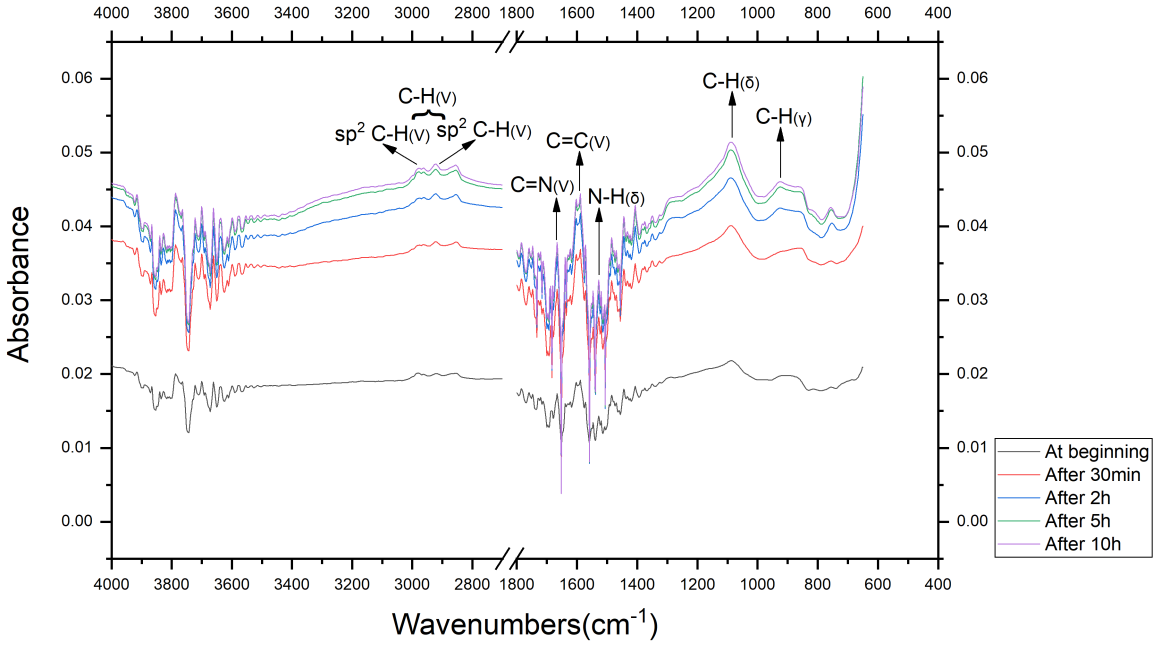

Figure 62: In-situ FTIR spectra of copper in 100ml 1 mM 1H-HB-2T solution.

The change of peak intensity in 1 mM 1H-HB-2T THF solution is the same as that in the MBI THF solution. They increase quickly for the first 5 hours and then rise at a small rate. The adsorption process finishes in 5 hours and then surface equilibrium has achieved.

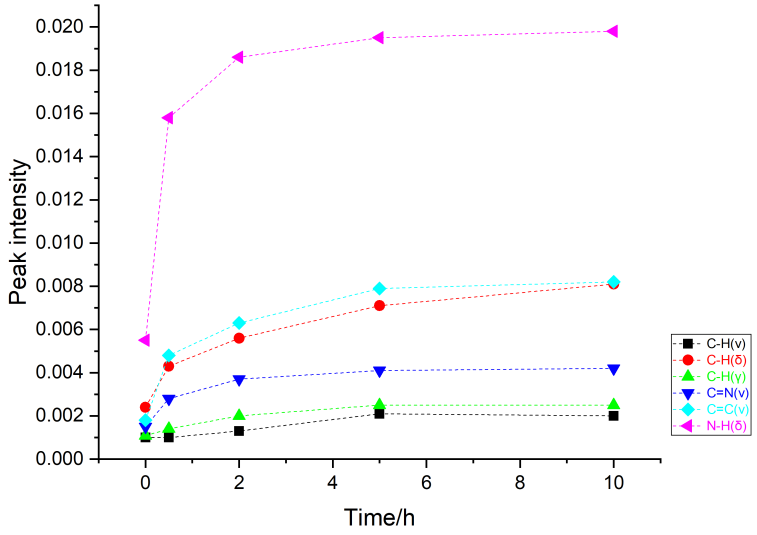

Figure 63: Peak intensity values of Zn from 1H-HB-2T FTIR spectra.

3.2.3 Summary of FTIR measurements

In ex-situ FTIR measurements, most kinds of functional groups of MBI and 1H-HB-2T are observed. Among these functional groups, the unexpected N-H bond of 1H-HB-2T indicates a spontaneous structure transformation from thiol to thione, N and S atoms are the most possible atoms bonding with metallic surfaces, but it is difficult to affirm their detailed function. In-situ FTIR results are very similar and prove that the adsorption process of both inhibitors could reach an equilibrium state within 5 hours.

4 Conclusion

Corrosion inhibition properties of two organic compounds, 2-mercapto-benzimidazole (MBI) and 2-mercapto-1-methyl-benzimidazole (1H-HB-2T), on copper alloys (brasses), are investigated in this thesis. Electrochemical measurements including linear polarization resistance (LPR) and electrochemical impedance spectroscopy (EIS) were utilized to study the corrosion inhibition performance and mechanisms of MBI and 1H-HB-2T for brasses. Then, ex-situ and in-situ Fourier transform infrared spectroscopy (FTIR) measurements were used to investigate the adsorption process and mechanisms of inhibitor molecules on the metallic surfaces. For brasses, the phase type directly determines the corrosion resistance of brass in the presence of organic inhibitors studied here. According to electrochemical measurement results,

The phase type of the brass substrate is one of the most important factors determining the corrosion resistance in the presence of organic inhibitors studied here. It was shown that the alpha-phase brasses (10% Zn brass and 30% Zn brass) have the highest corrosion resistance in the presence of studied inhibitors. With an increased zinc content, the corrosion resistance of brass decreases except for the gamma-phase brass specimens containing 60% Zn.

Although MBI and 1H-HB-2T have similar chemical structures, 1H-HB-2T shows better corrosion inhibition than MBI owing to its extra methyl functional group. Moreover, 1H-HB-2T possibly has a spontaneous structure transformation from thiol to thione. The interaction mechanisms of MBI and 1H-HB-2T molecules on copper and brass are most likely to be chemisorption, but the chemical bond formation mode is still a question. Additionally, the absorption process of the inhibitors on the metallic sufaces take place in 5 hours.

5 Future work

Based on the results of this thesis, further researches could be conducted from the following several aspects.

1. The roles of S and N atoms in the bonding formation process are still unclear. Although there already are some modeling and calculations, an experimental evidence is still missing.
2. The brass specimens studied in this thesis are based on copper-zinc alloys showing different interactions with the inhibitors. Other types of copper alloys with Pb, Sn and Mn alloying elements included could be a future work.

6 Acknowledgement

First I would like to express my sincere gratitude to my supervisors, Prof. J.M.C. Mol and Dr. P. Taheri, not only for their guidance, support and understanding on my thesis but also for their lasting help during my corrosion study.

Special thanks are also directed to members of our corrosion group for their valuable advice and friendly help during my thesis. A very special thanks go to the technician Agnieszka who helps me with experiments since the beginning of my thesis.

Lastly, I would like to thank my family for their patience and encouragement. Thanks to their thoughtful kindness, I can cheer up from the trough again and again.

I think the two-year study at TU Delft is a precious development experience for both my personality and academic ability. As one important part of the master program, the thesis built a solid foundation for my next PhD study. And I believe what I learned here will positively shape my entire life. Sincere thanks to all you once again.

References

[1] Volkan Cicek and Bayan Al-Numan. *Corrosion chemistry*. John Wiley & Sons, 2011.

[2] LL Shreir, RA Jarman, and GT Burstein. Corrosion: Volume 1, 1994.

[3] David EJ Talbot and James DR Talbot. *Corrosion science and technology*. CRC press, 2018.

[4] NFMN Cabrera and Nevill Francis Mott. Theory of the oxidation of metals. *Reports on progress in physics*, 12(1):163, 1949.

[5] Daniel B Miracle, Steven L Donaldson, Scott D Henry, Charles Moosbrugger, Gayle J Anton, Bonnie R Sanders, Nancy Hrivnak, Carol Terman, Jill Kinson, Kathryn Muldoon, et al. *ASM handbook*, volume 21. ASM international Materials Park, OH, USA, 2001.

[6] wikipedia. https://en.wikipedia.org/wiki/brass.

[7] Damien Féron. *Corrosion behaviour and protection of copper and aluminium alloys in seawater*, volume 50. Elsevier, 2007.

[8] TP Hoar and CJL Booker. The electrochemistry of the stress-corrosion cracking of alpha brass. *Corrosion Science*, 5(12):821–840, 1965.

[9] John Michael West. Basic corrosion and oxidation. 1986.

[10] Omnia S Shehata, Lobna A Korshed, and Adel Attia. Green corrosion inhibitors, past, present, and future. *Corrosion Inhibitors, Principles and Recent Applications*, page 121, 2018.

[11] Camila G Dariva and Alexandre F Galio. Corrosion inhibitors–principles, mechanisms and applications. In *Developments in corrosion protection*, page 370. IntechOpen, 2014.

[12] JB Lumsden and Z Szklarska-Smialowska. The properties of films formed on iron exposed to inhibitive solutions. *Corrosion*, 34(5):169–176, 1978.

[13] R Heiyantuduwa, MG Alexander, and JR Mackechnie. Performance of a penetrating corrosion inhibitor in concrete affected by carbonation-induced corrosion. *Journal of materials in civil engineering*, 18(6):842–850, 2006.

[14] Zhou Baiqing, Wang Xiaowei, Li Qin, and Peng Yisheng. Performance and mechanism of a water stabiliser for low hardness cooling water. *Anti-Corrosion Methods and Materials*, 50(5):347–351, 2003.

[15] Danick Gallant and Stéphan Simard. A study on the localized corrosion of cobalt in bicarbonate solutions containing halide ions. *Corrosion science*, 47(7):1810–1838, 2005.

[16] V GENTIL. Corrosão. 4. a edição, ed. *LTC: Rio de Janeiro*, 2003.

[17] Arthur W Adamson, Alice Petry Gast, et al. *Physical chemistry of surfaces*, volume 15. Interscience New York, 1967.

[18] J Aljourani, K Raeissi, and MA Golozar. Benzimidazole and its derivatives as corrosion inhibitors for mild steel in 1m hcl solution. *Corrosion science*, 51(8):1836–1843, 2009.

[19] Aprael S Yaro, Anees A Khadom, and Rafal K Wael. Apricot juice as green corrosion inhibitor of mild steel in phosphoric acid. *Alexandria Engineering Journal*, 52(1):129–135, 2013.

[20] Stanley E Manahan. Fundamentals of environmental chemistry. 1993.

[21] Sha Cheng, Shougang Chen, Tao Liu, Xueting Chang, and Yansheng Yin. Carboxymenthylchitosan as an ecofriendly inhibitor for mild steel in 1 m hcl. *Materials Letters*, 61(14-15):3276–3280, 2007.

[22] J Cruz, R Martınez, J Genesca, and E Garcıa-Ochoa. Experimental and theoretical study of 1-(2-ethylamino)-2-methylimidazoline as an inhibitor of carbon steel corrosion in acid media. *Journal of Electroanalytical Chemistry*, 566(1):111–121, 2004.

[23] Ingrid Milošev, Nataša Kovačević, and Anton Kokalj. Effect of mercapto and methyl groups on the efficiency of imidazole and benzimidazole-based inhibitors of iron corrosion. *Acta Chimica Slovenica*, 63(3):544–559, 2016.

[24] Zhengwei Liu, Tracey S Jackson, and Jacob Gibson. Low dosage chemical suppression agents for carbon steels degradation, January 4 2018. US Patent App. 15/637,657.

[25] Allen J Bard, Larry R Faulkner, Johna Leddy, and Cynthia G Zoski. *Electrochemical methods: fundamentals and applications*, volume 2. wiley New York, 1980.

[26] Milton Stern and Al L Geary. Electrochemical polarization i. a theoretical analysis of the shape of polarization curves. *Journal of the electrochemical society*, 104(1):56–63, 1957.

[27] R Winston Revie. *Corrosion and corrosion control: an introduction to corrosion science and engineering*. John Wiley & Sons, 2008.

[28] D Needham. Reverse engineering of the low temperature-sensitive liposome (ltsl) for treating cancer. In *Biomaterials for Cancer Therapeutics*, pages 270–353e. Elsevier, 2013.

[29] Optieis: A multisine implementation application note rev. 1.0. 1990-2011.

[30] Vadim F Lvovich. *Impedance spectroscopy: applications to electrochemical and dielectric phenomena*, page 4. John Wiley & Sons, 2012.

[31] JB Bates. Fourier transform infrared spectroscopy. *Science*, 191(4222):31–37, 1976.

[32] JL Koening, SQ Wang, and R Bhargava. Ftir images: a new technique produces images worth a thousand spectra. *Anal. Chem*, 73:360A–369A, 2001.

[33] NJ Harrick. Determination of refractive index and film thickness from interference fringes. *Applied optics*, 10(10):2344–2349, 1971.

[34] Milan Milosevic and Sean W King. Analysis of low-k dielectric thin films on thick substrates by transmission ftir spectroscopy. *ECS Journal of Solid State Science and Technology*, 4(1):N3146–N3152, 2015.

[35] Tatiana Konevskikh, Arkadi Ponossov, Reinhold Blümel, Rozalia Lukacs, and Achim Kohler. Fringes in ftir spectroscopy revisited: understanding and modelling fringes in infrared spectroscopy of thin films. *Analyst*, 140(12):3969–3980, 2015.

[36] DR Vij. *Handbook of applied solid state spectroscopy*, pages 411–446. Springer Science & Business Media, 2007.

[37] Huaiyu Wang and Paul K Chu. Surface characterization of biomaterials. In *Characterization of biomaterials*, pages 105–174. Elsevier, 2013.

[38] Roland W Bittner and Helmuth Hoffmann. Surface analysis | infrared spectroscopy. 2019.

[39] G Kear, BD Barker, and FC Walsh. Electrochemical corrosion of unalloyed copper in chloride media—-a critical review. *Corrosion science*, 46(1):109–135, 2004.

[40] Tadeja Kosec, Ingrid Milošev, and Boris Pihlar. Benzotriazole as an inhibitor of brass corrosion in chloride solution. *Applied Surface Science*, 253(22):8863–8873, 2007.

[41] Nataša Kovačević, Ingrid Milošev, and Anton Kokalj. The roles of mercapto, benzene, and methyl groups in the corrosion inhibition of imidazoles on copper: Ii. inhibitor–copper bonding. *Corrosion Science*, 98:457–470, 2015.

[42] SS Mahmoud. Corrosion inhibition of iron by amphoteric surfactants in hydrochloric acid solutions. *Journal of materials science*, 42(3):989–997, 2007.

[43] Donald L Pavia, Gary M Lampman, George S Kriz, and James A Vyvyan. *Introduction to spectroscopy*. Cengage Learning, 2008.

[44] Mohammed R Ahamed, Shetha F Narren, and Amal S Sadiq. Synthesis of 2-mercaptobenzimidazole and some of its derivatives. *Al-Nahrain Journal of Science*, 16(2):77–83, 2013.

[45] Thomas G Mayerhöfer and Jürgen Popp. The electric field standing wave effect in infrared transflection spectroscopy. *Spectrochimica Acta Part A: Molecular and Biomolecular Spectroscopy*, 191:283–289, 2018.